A new SMAP soil moisture and vegetation optical depth product (SMAP-IB): Algorithm, assessment and inter-comparison

Xiaojun Li, Jean-Pierre Wigneron, Lei Fan, Frédéric Frappart, Simon H Yueh, Andreas Colliander, Ardeshir Ebtehaj, Lun Gao, Roberto Fernandez-Moran, Xiangzhuo Liu, et al.

Remote Sensing of Environment 271 (2022) 112921

Contents lists available at ScienceDirect

Remote Sensing of Environment

journal homepage: www.elsevier.com/locate/rse

A new SMAP soil moisture and vegetation optical depth product (SMAP-IB): Algorithm, assessment and inter-comparison

Xiaojun Li [a], Jean-Pierre Wigneron [a,*], Lei Fan [b], Frédéric Frappart [a], Simon H. Yueh [c], Andreas Colliander [c], Ardeshir Ebtehaj [d], Lun Gao [d], Roberto Fernandez-Moran [e], Xiangzhuo Liu [a], Mengjia Wang [a,f], Hongliang Ma [a,g], Christophe Moisy [a], Philippe Ciais [h]

[a] INRAE, UMR1391 ISPA, Université de Bordeaux, F-33140 Villenave d'Ornon, France
[b] Chongqing Jinfo Mountain Karst Ecosystem National Observation and Research Station, School of Geographical Sciences, Southwest University, Chongqing 400715, China
[c] Jet Propulsion Laboratory, California Institute of Technology, 4800 Oak Grove Drive, Pasadena CA91109, USA
[d] Saint Anthony Falls Laboratory, Department of Civil Environmental and Geo-Engineering, University of Minnesota, Minneapolis, MN 55414, United States
[e] University of Valencia, Image Processing Lab (IPL), Valencia, Spain
[f] State Key Laboratory of Remote Sensing Science, Faculty of Geographical Science, Beijing Normal University, Beijing 100875, China
[g] State Key Laboratory of Information Engineering in Surveying, Mapping, and Remote Sensing, Wuhan University, Wuhan 430079, China
[h] Laboratoire des Sciences du Climat et de l'Environnement, CEA/CNRS/UVSQ/Université Paris Saclay, Gif-sur-Yvette, France

ARTICLE INFO

Editor: Jing M. Chen

Keywords:
SMAP
L-MEB
Soil moisture
Vegetation optical depth
SMAP-IB
Biomass
Evaluation

ABSTRACT

Passive microwave remote sensing at L-band (1.4 GHz) provides an unprecedented opportunity to estimate global surface soil moisture (SM) and vegetation water content (via the vegetation optical depth, VOD), which are essential to monitor the Earth water and carbon cycles. Currently, only two space-borne L-band radiometer missions are operating: the Soil Moisture and Ocean Salinity (SMOS) and the Soil Moisture Active Passive (SMAP) missions in orbit since 2009 and 2015, respectively. This study presents a new mono-angle retrieval algorithm (called SMAP-INRAE-BORDEAUX, hereafter SMAP-IB) of SM and L-band VOD (L-VOD) from the dual-channel SMAP radiometric observations. The retrievals are based on the L-MEB (L-band Microwave Emission of the Biosphere) model which is the forward model of SMOS-IC and of the official SMOS retrieval algorithms. The SMAP-IB product aims at providing good performances for both SM and L-VOD while remaining independent of auxiliary data: neither modelled SM data nor optical vegetation indices are used as input in the algorithm. Inter-comparison with other SM and L-VOD products (i.e., MT-DCA, SMOS-IC, and the new versions of DCA and SCA-V extracted from SMAP passive Level 3 product) suggested that SMAP-IB performed well for both SM and L-VOD. In particular, SMAP-IB SM retrievals presented the higher scores ($R = 0.74$) in capturing the temporal trends of *in-situ* observations from ISMN (International Soil Moisture Network) during April 2015–March 2019, followed by MT-DCA ($R = 0.71$). While the lowest *ub*RMSD value was obtained by the new version of SMAP DCA (0.056 m^3/m^3), SMAP-IB SM retrievals presented best scores for R, *ub*RMSD ($\sim$ 0.058 m^3/m^3) and bias (0.002 m^3/m^3) when considering only products independent of optical vegetation indices (e.g., NDVI). L-VOD retrievals from SMAP-IB, MT-DCA, and SMOS-IC were well correlated (spatially) with aboveground biomass and tree height, with spatial R values of $\sim$0.88 and $\sim$ 0.90, respectively. All three L-VOD products exhibited a smooth non-linear density distribution with biomass and a good linear relationship with tree height, especially at high biomass levels, while the L-VOD datasets incorporating optical information in the algorithms (i.e., SCA-V and DCA) showed obvious saturation effects. It is expected that this new algorithm can facilitate the fusion of both SM and L-VOD retrievals from SMOS and SMAP to obtain long-term and continuous L-band earth observation products.

* Corresponding author.
E-mail address: jean-pierre.wigneron@inrae.fr (J.-P. Wigneron).

https://doi.org/10.1016/j.rse.2022.112921
Received 30 August 2021; Received in revised form 29 November 2021; Accepted 21 January 2022
Available online 2 February 2022

1. Introduction

Global monitoring of surface soil moisture (SM) and vegetation features from space is essential to better understand the water (Koster et al., 2004), energy fluxes (Anderson et al., 2008), and carbon cycles (Liu et al., 2015; Jung et al., 2017) as well as to improve weather predictions (Tuttle and Salvucci, 2016) and management of water and food resources (Dobriyal et al., 2012). Passive microwave remote sensing at low frequencies, especially at L-band (1.4 GHz), provides an unprecedented opportunity to estimate SM and vegetation water content (via vegetation optical depth, VOD) from regional to global scales due to its high sensitivity to surface dielectric properties, deep penetration into vegetation, frequent revisits (i.e., every 2–3 days globally) and all-weather sensing capability (Schmugge et al., 1986; Jackson et al., 2010; Kurum, 2013; Wigneron et al., 2017). Currently, only two space-borne L-band radiometer missions are in operation: Soil Moisture and Ocean Salinity (SMOS) developed by European Space Agency (ESA) and Soil Moisture Active Passive (SMAP) developed by National Aeronautics and Space Administration (NASA) (Kerr et al., 2010; Entekhabi et al., 2010a).

The SMOS mission, launched on November 2, 2009, is equipped with a large Y-shaped interferometric radiometer allowing dual-polarized and multi-angular brightness temperature (TB) observations (Kerr et al., 2010). This observational capability is the key to simultaneously retrieving SM and L-band vegetation optical depth at nadir (L-VOD) (Wigneron et al., 2000, 2007; Kerr et al., 2012). Currently, there are three main physically-based SMOS SM and L-VOD retrieval products available: SMOS level 2 (L2) (Kerr et al., 2012), SMOS level 3 (L3) (Al Bitar et al., 2017) and SMOS-IC (Fernandez-Moran et al., 2017b; Wigneron et al., 2021). The three different SMOS SM and L-VOD retrieval algorithms are all based on the inversion of the L-band Microwave Emission of the Biosphere (L-MEB) model (Wigneron et al., 2007), which used the τ-ω radiative transfer equation to simulate the land surface microwave emission. The development history, rationale and objectives of these three SMOS products are related to a certain extent (see Wigneron et al., 2021 for a review and more details on that topic), of which SMOS-IC is the latest one.

Relative to the multi-angular configuration of SMOS, the SMAP instrument launched on January 31, 2015 only provides mono-angular TB observations with a full-polarization mode at the incidence angle θ of 40° (Entekhabi et al., 2010a). Single-angle observations render more difficult simultaneous retrievals of SM and L-VOD as the Horizontal (H-) and Vertical (V-) polarized TB may contain shared information, which leads to ill-posed nonlinear inverse problems (Konings et al., 2017; Ebtehaj and Bras, 2019). The current SMAP inversion algorithms (available products) are mainly divided into two categories depending on the number of polarization observations used: the single-channel algorithm (SCA) (Jackson, 1993) and the dual-channel algorithm (DCA) (Njoku and Entekhabi, 1996; Njoku et al., 2003). SCA only retrieves SM using H or V polarization of TB as inputs, while L-VOD, as a key ancillary data for the SM retrievals, is estimated based on the climatology of the normalized difference vegetation index (NDVI) data (Jackson et al., 1999; Chan et al., 2013). In contrast, DCA retrieves both SM and L-VOD simultaneously based on a nonlinear least-squares minimization process using both the H and V polarization channels (Crow et al., 2005; O'Neill et al., 2015; Wigneron et al., 1993). However, after comparing these different algorithms, the classic DCA was found to provide noisier SM (Chan et al., 2016; Konings et al., 2017) and the SMAP official SM baseline algorithm is initially SCA based on the V polarization (SCA-V) (O'Neill et al., 2020).

Since L-VOD is considered as a promising ecological indicator (Frappart et al., 2020; Konings et al., 2017; Tian et al., 2018) and direct retrievals of L-VOD could alleviate propagation of uncertainty of ancillary data into the SM retrievals (Chaubell et al., 2020; Dong et al., 2018), several advanced DCA algorithms have been proposed for retrieving SM and L-VOD from the SMAP data. According to the different technologies used to reduce the uncertainty in the classic DCA inversion process, these algorithms can be classified between spatio-temporal constrained algorithms and regularized DCA ones (Gao et al., 2021). The spatio-temporal constrained algorithms use additional information from multi-temporal or spatial observation to resolve the under-determined problem of the SMAP classic DCA algorithm (Konings et al., 2017; Karthikeyan et al., 2019), including the multi-temporal dual channel algorithm (MT-DCA) (Konings et al., 2016), the constrained multi-channel algorithm (CMCA) (Ebtehaj and Bras, 2019), the combined CMCA (C-CMCA) (Gao et al., 2020a), and the spatially CMCA (S-CMCA) (Gao et al., 2020b). Specifically, MT-DCA retrieves SM, L-VOD and single scattering albedo using a 7-day time window of TB observations—over which, it is assumed that L-VOD remains constant (Konings et al., 2017). However, this assumption contrasts with recent studies that showed non-negligible L-VOD changes over the day following rainfall events (Feldman et al., 2018; Wigneron et al., 2021), leading to the development of the "CMCA" type algorithms, which also constrain the physical bounds of SM and the climatological range of L-VOD derived from optical data sources (Gao et al., 2021). More recently, a modified DCA algorithm (MDCA) was also proposed (O'Neill et al., 2020) in which the cost function is augmented by an additional regularization term incorporating *a priori* information from NDVI to prevent noise amplification.

However, *a priori* information should be used with caution as it: i) may bring uncertainty to the retrievals (Gao et al., 2020c; Wigneron et al., 2017); ii) makes the final product not independent of it by integrating its content in a hidden way (Fernandez-Moran et al., 2017b; Wigneron et al., 2021). As a consequence, the direct use of VOD climatology derived from MODIS (Moderate Resolution Imaging Spectroradiometer) NDVI to represent the L-VOD value (τ) in SMAP SCA could fail to represent the real-time dynamics of L-VOD and cause subsequently errors in the SCA SM retrievals (Gao et al., 2020c; Dong et al., 2018; Zwieback et al., 2018). Besides, most of the aforementioned DCA algorithms use MODIS NDVI-based VOD climatology as initial guess for retrieving (O'Neill et al., 2020) or determining the physical range (Ebtehaj and Bras, 2019) of L-VOD. This undoubtedly limits the consideration of L-VOD and optical vegetation indices as independent proxies for monitoring the vegetation dynamics such as phenology and carbon cycle, as the retrieved L-VOD is, in this case, not completely independent of the optical data (Li et al., 2021). In addition, integration of optical vegetation indices in the L-VOD retrieval, may bring circularity when evaluating remotely-sensed products against modelled ones (Wigneron et al., 2021).

In contrast, SMOS-IC was developed with the objective of simplifying the input of the L-MEB model by not using any external hydrologic or vegetation products, making the SMOS-IC product very interesting for inter-comparison analyses and robust applications (Wigneron et al., 2021). Using *in-situ* measurements, recent inter-comparisons with other passive products have showed the good performances of the SMOS-IC SM product (Al-Yaari et al., 2019; Ma et al., 2019). Higher spatial correlations were also found between SMOS-IC L-VOD and vegetation-related features (aboveground biomass, tree height and vegetation indices) than other products (Rodríguez-Fernández et al., 2018; Li et al., 2021). Benefiting from this, the SMOS-IC L-VOD with an 11-year global dataset has been widely used for monitoring the vegetation seasonality (Tian et al., 2018; Al-Yaari et al., 2020; Li et al., 2021) and aboveground carbon stocks (Brandt et al., 2018; Fan et al., 2019; Tong et al., 2020; Wigneron et al., 2020; Qin et al., 2021; see Wigneron et al., 2021 for a review). Therefore, extending the use of the L-MEB inversion approach from the SMOS retrievals to the SMAP retrievals appears to be potentially very interesting. First, it would allow obtaining microwave products that are independent of any modelled SM products or optical vegetation indexes. Second, it would contribute to facilitate the fusion of both SM and L-VOD retrievals from SMOS and SMAP to obtain long-term and continuous L-band earth observation products. However, this fusion is still hindered as the aforementioned SMOS and SMAP algorithms are

different and are developed for different objectives. For instance, SCA-V is dedicated to the quality of SM (Chan et al., 2016; O'Neill et al., 2020), while MT-DCA is focused more on the performance of L-VOD (Konings et al., 2017; Bai et al., 2019). In general, there is still a lack of mono-angle (SMAP or SMOS) retrieval algorithm that considers the performance of both SM and L-VOD while remaining relatively independent of auxiliary data, i.e., optical observations.

In this context, a new algorithm based on the inversion of the L-MEB forward emission model to retrieve both SM and L-VOD from SMAP data is proposed in present study, called SMAP-INRAE-BORDEAUX (SMAP-IB). The main objectives of the SMAP-IB product are (i) searching for good performances in both the SM and L-VOD products, instead of focusing on the quality of only one of them; (ii) remaining independent of hydrologic and vegetation auxiliary data, as done currently in SMOS-IC. To cope with the under-determined problem of retrieving two parameters from only two correlated SMAP observations, the cost function of SMAP-IB imposes constraints on both SM and L-VOD by using previous multi-temporal retrieval information to initialize the corresponding retrievals (See Section 2.2.2). This paper aims at presenting the SMAP-IB algorithm and illustrating the main features of the SMAP-IB SM and L-VOD products at the global scale, in comparison to SMOS-IC V2 as well as to the three other SMAP products, including MT-DCA and the recent SMAP passive Level 3 products retrieved from SCA-V and the regularized MDCA (O'Neill et al., 2020). To achieve this, all five SM products were inter-compared against the International Soil Moisture Network (ISMN) *in-situ* measurements from April 2015 to March 2019, while the L-VOD products were compared to NDVI, canopy height (Lang et al., 2021) and AGB datasets (Saatchi et al., 2011).

This paper is organized as follows: the used datasets and the SMAP-IB algorithm are described in Section 2. In Section 3, the performance of SMAP-IB SM and L-VOD retrievals are inter-compared with the four other products. Discussions about the limitations and potential improvements of SMAP-IB are presented in Section 4. Concluding remarks and outlook are given in Section 5.

2. Materials and methods

2.1. Datasets

2.1.1. SMAP Level3 TB products

The SMAP-IB retrieval algorithm was applied to four years of brightness temperatures (TB) from the SMAP level-3 (L3) passive product (SPL3SMP, Version 7) from April 2015 to March 2019. The daily SPL3SMP TB product, obtained from the NSIDC (National Snow and Ice Data Center), consists of Horizontally (H-) and Vertically (V-) polarized brightness temperatures observed at an incidence angle θ of 40° (O'Neill et al., 2020). The dataset is projected on a global cylindrical Equal Area Scalable Earth Grid version 2.0 (EASE-Grid 2.0), with a grid sampling resolution of 36 km. The SPL3SMP is a daily composite of the SMAP passive level 2 half-orbit product, which contains gridded TB data of both descending (06:00 am local time) and ascending (06:00 pm local time) SMAP radiometer-based observations and quality-assessment flags (O'Neill et al., 2020). In this study, only TB observations with acceptable quality flags acquired at descending orbit were used. SPL3SMP is freely available at https://nsidc.org/data/SPL3SMP/versions/7.

2.1.2. ECMWF ERA5 reanalysis data

We used the ECMWF modelled SM of the soil layer 1 (top 0–7 cm), the skin temperature, and the soil temperatures of layer 1 (0–7 cm) and layer 3 (28–100 cm). These hourly ECMWF variables were derived from the ERA5 reanalysis dataset, which is based on improved historical measurements and at a finer horizontal resolution (31 km) than its predecessor ERA-Interim (80 km) (Hersbach et al., 2020). ERA5 surface soil temperature also presents visible improvements compared to ERA-Interim (Ma et al., 2021). More details on the set-up of ERA5 can be found in Hersbach et al. (2020). ECMWF skin and soil temperatures from layers 1 and 3 were used to estimate the vegetation and soil effective temperatures of the SMAP-IB algorithm, while the reanalyzed SM was used to calibrate the model parameters (see Section 2.2.2). All these ECMWF variables were resampled to 36 km EASE-Grid 2.0 using the linear averaging method over the same study period. Recent evaluations show that ERA5 SM can well represent the global soil moisture variability (Hersbach et al., 2020) and it has higher scores than four other reanalysis SM products when compared against ground measurements (Li et al., 2020a).

2.1.3. ISMN in-situ SM measurements

To evaluate the skills of the SMAP-IB SM retrievals, *in-situ* SM data from the ISMN database were used (Dorigo et al., 2021). ISMN is an international cooperation to construct and maintain a global *in-situ* SM database, which is essential for promoting scientific studies on the calibration/validation and improvement of global remotely-sensed products as well as land surface models (Dorigo et al., 2013). Currently, the ISMN database (https://ismn.geo.tuwien.ac.at/en/) hosts SM field stations from ~60 networks mainly located over the US and Europe. In this study, only the top 0–5 cm of *in-situ* SM data from April 2015 to March 2019 with sufficiently long time series of observations were used. To close the resolution gap and ensure the accuracy of the *in-situ* SM data, only gauge measurements flagged as "Good" quality from the same network within a 36 km footprint were spatially averaged (Al-Yaari et al., 2019; Dorigo et al., 2013; Li et al., 2020b). Consequently, 19 networks (Table 1) covering a total of 417 SMAP footprints were retained from ISMN. Fig. 1 shows the locations of these SMAP footprints with a land cover classification map based on the International Geosphere Biosphere Programme (IGBP) schema as background.

2.1.4. Vegetation-related proxies for assessing L-VOD

Three vegetation parameters, including aboveground biomass (AGB), canopy height (as a proxy of the total amount of vegetation matter) and NDVI (as a proxy of the green vegetation cover and vegetation density), were selected to evaluate the SMAP-IB L-VOD retrievals. These vegetation parameters are related to the vegetation information expressed by VOD and are widely used for VOD evaluation and inter-comparison (Tian et al., 2016; Grant et al., 2016; Li et al., 2021; Wigneron et al., 2021). We refer the readers to Li et al. (2021), who globally assessed and inter-compared nine commonly used VOD products, for more details.

To investigate the spatial relationship between L-VOD and AGB, we used the AGB dataset representing aboveground biomass circa 2015 updated from Saatchi et al. (2011). The 1-km Saatchi AGB map is generated using multiple datasets sources, including ground-based inventory plots and satellite observations from Shuttle Radar Topography Mission (SRTM), ICESat, MODIS, and Quick Scatterometer (QSCAT). Saatchi AGB is considered here because it has been widely used as a benchmark to convert L-VOD to carbon density (Tong et al., 2020; Wigneron et al., 2020; Qin et al., 2021). In this study, we aggregated the static AGB dataset to 36 km by simple spatial averaging as suggested by Li et al. (2021) and Fan et al. (2019).

The 0.5-degree resolution LIDAR canopy height estimation made in 2019 from the Global Ecosystem Dynamics Investigation (GEDI) (Lang et al., 2021) is applied to evaluate the spatial correlation between L-VOD and vegetation height. This canopy height dataset is estimated based on the first four months (April – July 2019) of the GEDI Level 1B LIDAR waveforms and Bayesian deep learning with an RMSE accuracy of 2.7 m; more details about this dataset can be found in Lang et al. (2021). The latter dataset is selected mainly because the total vegetation amount is highly correlated with canopy height (Li et al., 2021). Moreover, as the first space-based LIDAR dedicated to measuring vertical forest structure, GEDI is expected to serve as an interesting source of information for AGB mapping (Silva et al., 2021) and canopy height estimation (Liu et al., 2021a).

To evaluate the seasonality of the L-VOD retrievals, we collected 16-

Table 1
List of *in-situ* networks from ISMN. The VOD level is defined according to the SMOS-IC L-VOD value as: VOD-I (0–0.1); VOD-II (0.1–0.2); VOD-III (0.2–0.3); VOD-IV (0.3–0.4); VOD-V (0.4–0.5) and VOD-VI (> 0.5).

Network name	Country	No. of footprints covered	IGBP land cover	VOD level	Reference
SCAN	USA	130	Diverse land cover types: ENF (1), DBF (6), MF (3), SH (14), WS (11), G (53), C (22), CNVM (17) and BSV (3)	Diverse VOD levels: VOD-I (22), VOD-II (44), VOD-III (31), VOD-IV (12), VOD-V (9) and VOD-VI (12)	(Schaefer et al., 2007)
SNOTEL	USA	130	Diverse land cover types: ENF (42), MF (1), SH (1), WS (4) and G (82)	Diverse VOD levels: VOD-I (3), VOD-II (34), VOD-III (31), VOD-IV (27), VOD-V (17) and VOD-VI (18)	(Serreze et al., 2001)
AMMA-CATCH	Benin, Niger	2	WS (1) and CNVM (1)	VOD-I (1) and VOD-II (1)	(Lebel et al., 2009)
DAHRA	Senegal	1	G (1)	VOD-I (1)	(Tagesson et al., 2015)
FR_Aqui	France	2	MF (1) and WS (1)	VOD-IV (2)	(Al-Yaari et al., 2018)
HOAL	Austria	1	MF (1)	VOD-V (1)	(Blöschl et al., 2016)
MAQU	China	4	G (4)	VOD-II (4)	(Su et al., 2011)
NAQU	China	2	G (2)	VOD-I (2)	
NGARI	China	1	BSV (1)	VOD-II (1)	
RISMA	Canada	6	C (5) and CNVM (1)	VOD-II (5) and VOD-III (1)	(http://aafc.fieldvision.ca/)
SMOSMANIA	France	17	MF (6), WS (1) and C (10)	Diverse VOD levels: VOD-II (4), VOD-III (7), VOD-IV (5) and VOD-V (1)	(Albergel et al., 2008)
SOILSCAPE	USA	3	SH (1) and WS (2)	VOD-I (1), VOD-III (1) and VOD-VI (1)	(Moghaddam et al., 2010)
TERENO	Germany	2	MF (1) and C (1)	VOD-III (1) and VOD-IV (1)	(Zacharias et al., 2011)
USCRN	USA	86	Diverse land cover types: ENF (5), DBF (3), MF (8), SH (7), WS (4), G (31), C (16), CNVM (11) and BSV (1)	Diverse VOD levels: VOD-I (15), VOD-II (25), VOD-III (17), VOD-IV (11), VOD-V (9) and VOD-VI (9)	(Bell et al., 2013)
HOBE	Denmark	2	C (2)	VOD-II (1) and VOD-III (1)	(http://www.hobe.dk/)
MySMNet	Malaysia	1	CNVM (1)	VOD-VI (1)	(Kang et al., 2019)
OZNET	Australia	7	G (4) and C (3)	VOD-I (4) and VOD-II (3)	(Smith et al., 2012)
REMEDHUS	Spain	3	C (3)	VOD-I (3)	(González-Zamora et al., 2019)
RSMN	Romania	17	C (15) and CNVM (2)	VOD-II (8), VOD-III (7) and VOD-IV (2)	(http://assimo.meteoromania.ro/)

Note: the number of stations/pixels included in each IGBP land cover or VOD level is also listed.

day NDVI data from the MODIS product (MOD13A2 Collection 6) for the same period (i.e., April 2015–March 2019), which is mapped on a 1 km × 1 km grid. As a proxy for vegetation greenness, NDVI is widely used not only for monitoring vegetation phenology (Hmimina et al., 2013), but for VOD inter-comparison, as these two vegetation variables have generally highly correlated seasonal cycles and interannual variations (Tian et al., 2018; Liu et al., 2011; Liu et al., 2021b; Wang et al., 2021). In this study, only NDVI observations flagged as "good quality" were retained as done by Li et al. (2021). The NDVI dataset was then resampled to 36 km applying the averaging method.

2.1.5. Other SM and L-VOD products used in the inter-comparison

To better appreciate the capability of the SMAP-IB SM and L-VOD retrievals, we inter-compared SMAP-IB with SMOS-IC as well as with three other SMAP products (i.e., MT-DCA, and the recent SMAP passive L3 products retrieved from regularized MDCA and SCA-V), which were all collected from April 2015 to March 2019 and aggregated to the 36 km EASE-Grid 2.0. Note that in the recent update (August 31, 2020) of the SMAP official products, in addition to the SM retrievals from SCA-V, two other optional algorithms were added: MDCA and SCA-H (O'Neill et al., 2020). As SCA-H and SCA-V are both single-channel algorithms and as SCA-V still performs better than SCA-H (Colliander et al., 2021), we only selected SCA-V and MDCA here for comparison. Moreover, to be consistent with the ATBD of the official SMAP product (i.e., rename "MDCA" to "DCA"), we also used the "SMAP DCA" term in this paper to refer to this updated algorithm instead of referring to the classic DCA. To the best of our knowledge, DCA will be soon updated to replace SCA-V as the baseline algorithm for SMAP SM retrieval (O'Neill et al., 2021). More details about these SM and L-VOD products are presented in Supplementary text.

2.1.6. Ancillary datasets

Several ancillary datasets aggregated to 36 km were also utilized in this study, including soil texture, land cover classification, and daily precipitation from the Global Precipitation Measurement (GPM) L3 product (Huffman et al., 2019; Long et al., 2020). The soil texture attributes in terms of clay fraction as input to SMAP-IB were compiled from the Harmonized World Soil Database and several regional datasets (Peng et al., 2019). In addition, to comprehensively evaluate SMAP-IB, the MODIS-based global land cover classification map (Fig. 1) with full details described in Brodzik and Knowles (2011) was used to analyze the inter-comparison results, as earlier studies have shown that the performance of the remotely-sensed SM (Al-Yaari et al., 2019; Ma et al., 2019; Bai et al., 2019) or VOD retrievals (Li et al., 2021; Rodríguez-Fernández et al., 2018) may vary as a function of the land cover types.

2.2. Methodology

The flow chart illustrating the methodology of this study is shown in Fig. 2, which consists of three steps: parameter calibration, SM and L-VOD production and the performance evaluation step.

2.2.1. The SMAP-IB forward model

The SMAP-IB algorithm is based on a 2-Parameter (i.e., SM and L-VOD) inversion of the L-band Microwave Emission of the Biosphere (L-MEB) model as defined in Wigneron et al. (2000, 2007). L-MEB, which has been progressively improved and refined since its first release (Wigneron et al., 2021; Wigneron et al., 2017), uses the Tau-Omega (τ-ω) radiative transfer model to simulate the land surface microwave emission expressed in terms of TB (Mo et al., 1982). The τ-ω model estimates above-canopy TB at p polarization (TB_p), where $p = \{H, V\}$, as a

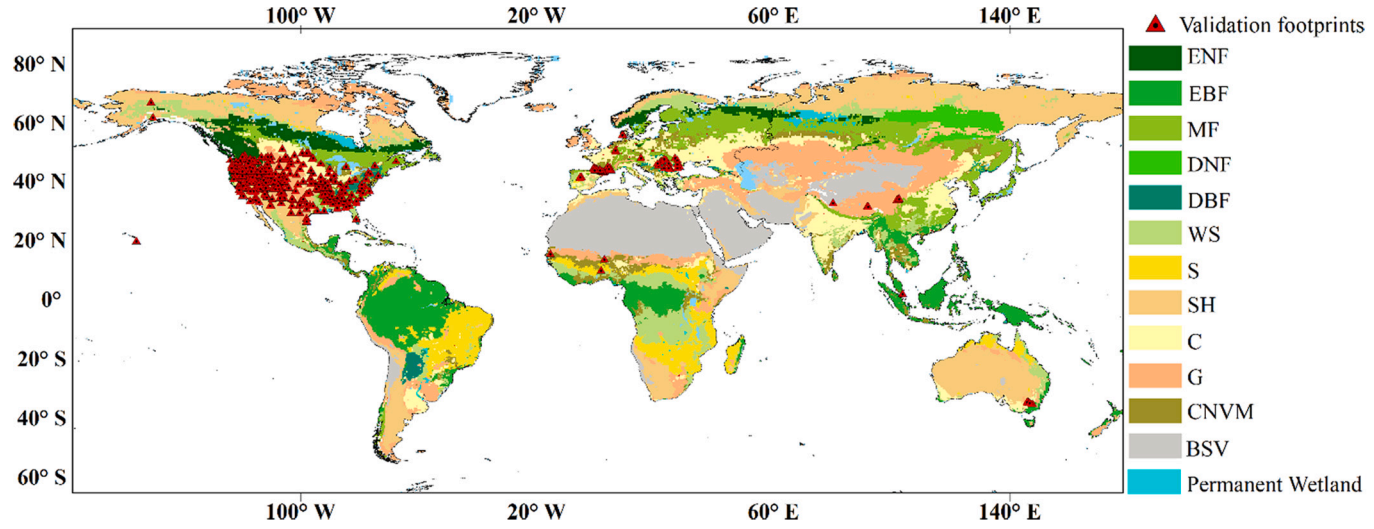

Fig. 1. Locations of the SMAP footprints used for validation. The overlaid MODIS land cover map is based on the IGBP classification scheme, which was aggregated to 36 km resolution by dominant class and combined into 12 vegetation types including ENF (Evergreen needleleaf forest), EBF (Evergreen broadleaf forest), MF (Mixed forests), DBF (Deciduous broadleaf forest), DNF (Deciduous needleleaf forest), WS (Woody savannas), S (Savannas), CNVM (Cropland/natural vegetation mosaics), SH (Open Shrublands and Closed Shrublands), C (Croplands), G (Grasslands), and BSV (Barren or sparsely vegetated).

sum of three components: (1) direct upwelling emission from soil and attenuated by the canopy $T_G(1-r_{Gp})\gamma_p$; (2) direct upwelling emission from canopy $T_C(1-\omega)(1-\gamma_p)$; and (3) downwelling emission from canopy reflected upwards by soil $Tc(1-\omega)(1-\gamma_p)r_{Gp}\gamma_p$:

$$TB_p = T_G(1-r_{Gp})\gamma_p + T_C(1-\omega)(1-\gamma_p) + T_C(1-\omega)(1-\gamma_p)r_{Gp}\gamma_p \quad (1)$$

where T_G and T_C are the effective temperature of soil and vegetation (K), which are, respectively, estimated from ERA5 soil and skin temperatures following the parameterization method of Wigneron et al. (2001, 2007); ω represents the effective scattering albedo, which is usually assumed polarization-independent (Kurum, 2013); γ_p represents the slanted vegetation attenuation factor (also called vegetation transmissivity), which is also assumed to be isotropic and polarization-independent. The vegetation attenuation can be described as a function of L_VOD (τ) and the incidence angle (θ) via $\gamma_p = \exp(-L\_VOD/cos\theta)$. The parameter r_{Gp} is the rough soil reflectivity at polarization p and is estimated through a semi-empirical model as suggested by Wigneron et al. (2007) including two components: the smooth soil reflectivity (r^*_{Gp}) and the roughness effects parameterized by H_R and N_{Rp} ($p = \{H, V\}$). In SMAP-IB, we used the values of ω, H_R, and N_{Rp} calibrated for SMOS-IC (Fernandez-Moran et al., 2017a; Parrens et al., 2016), and the values of ω were assigned as a function of the IGBP land cover types (Table S1). Table S1 also contains the values of ω proposed by the other algorithms involved in this study.

2.2.2. Retrieval of SM and L-VOD

The retrieval process of SMAP-IB is achieved by minimizing the following cost function (CF) that includes the squared weighted differences between observed (TB_p^{mes}) and simulated TB (TB_p^*) using a generalized least-squares iterative algorithm modified to account for *a priori* information available on the model input parameters (Wigneron et al., 2007):

$$CF = \frac{\sum\left(TB_p^{mes} - TB_p^*\right)^2}{\sigma(TB)^2} + \frac{(SM^{ini} - SM^*)^2}{\sigma(SM)^2} + \frac{(L\_VOD^{ini} - L\_VOD^*)^2}{\sigma(L\_VOD)^2} \quad (2)$$

where SM^* (L_VOD^*) is the value of the retrieved soil moisture (vegetation optical depth); σ_{SM} (σ_{L_VOD}) is the standard deviation of SM (L-VOD).

To alleviate the possible ill-conditioning issue due to highly correlated H- and V-polarized SMAP TB observations, three kinds of *a priori* information were used in Eq. (2) to constrain the SMAP-IB inversion process:

i) a constraint based on the initial value (or "first guess") of SM retrieval was added, i.e., item SM^{ini};
ii) a constraint based on the initial guess of L-VOD retrieval was added, i.e., item L_VOD^{ini};
iii) multi-temporal (MT) information was incorporated into the algorithm.

Among these three different items, the first two are considered in Eq. (2), while the third item (MT approach) is implicit during the optimization of SM^{ini} and L_VOD^{ini} and the corresponding σ_{SM} and σ_{L_VOD}. Specifically, the MT approach was developed to take into account the fact that L-VOD changes relatively slowly over time, as originally used in the SMOS retrieval algorithm (Wigneron et al., 2000), and as widely used later by several algorithms (e.g., SMOS L3 (Kerr et al., 2016); SMAP MT-DCA (Konings et al., 2017); SMOS-IC V2 (Wigneron et al., 2021), and AMSR-E sensor-based algorithm (Karthikeyan et al., 2019)). The relatively slow temporal change of L-VOD can be used as an extra constraint in the retrieval process of SM and VOD, and this constraint takes various forms (based on different assumptions) in different algorithms. For instance, MT-DCA incorporates the temporal observations of the TB values over a window of time by assuming L-VOD is time-invariant. In contrast, SMOS-IC V2 uses the averaged L-VOD retrievals from the previous (over a 10-day period) days as L_VOD^{ini} and also assigns a strong constraint on L-VOD ($\sigma_{L\_VOD} = 0.05$) to achieve the above assumption (Wigneron et al., 2021). In SMAP-IB, we adopted the same MT strategy as in the development of SMOS-IC V2, but we used it for SM too. Specifically, to retrieve SM and L-VOD at a date t (i.e., $SM^*(t)$ and $L\_VOD^*(t)$), we computed $SM^{ini}(t)$ and $L\_VOD^{ini}(t)$, respectively, as the mean values of SM^* and L_VOD^* retrieved from the previous w days (these previous dates are represented here as t_{-1}, t_{-2}, … t_{-w}):

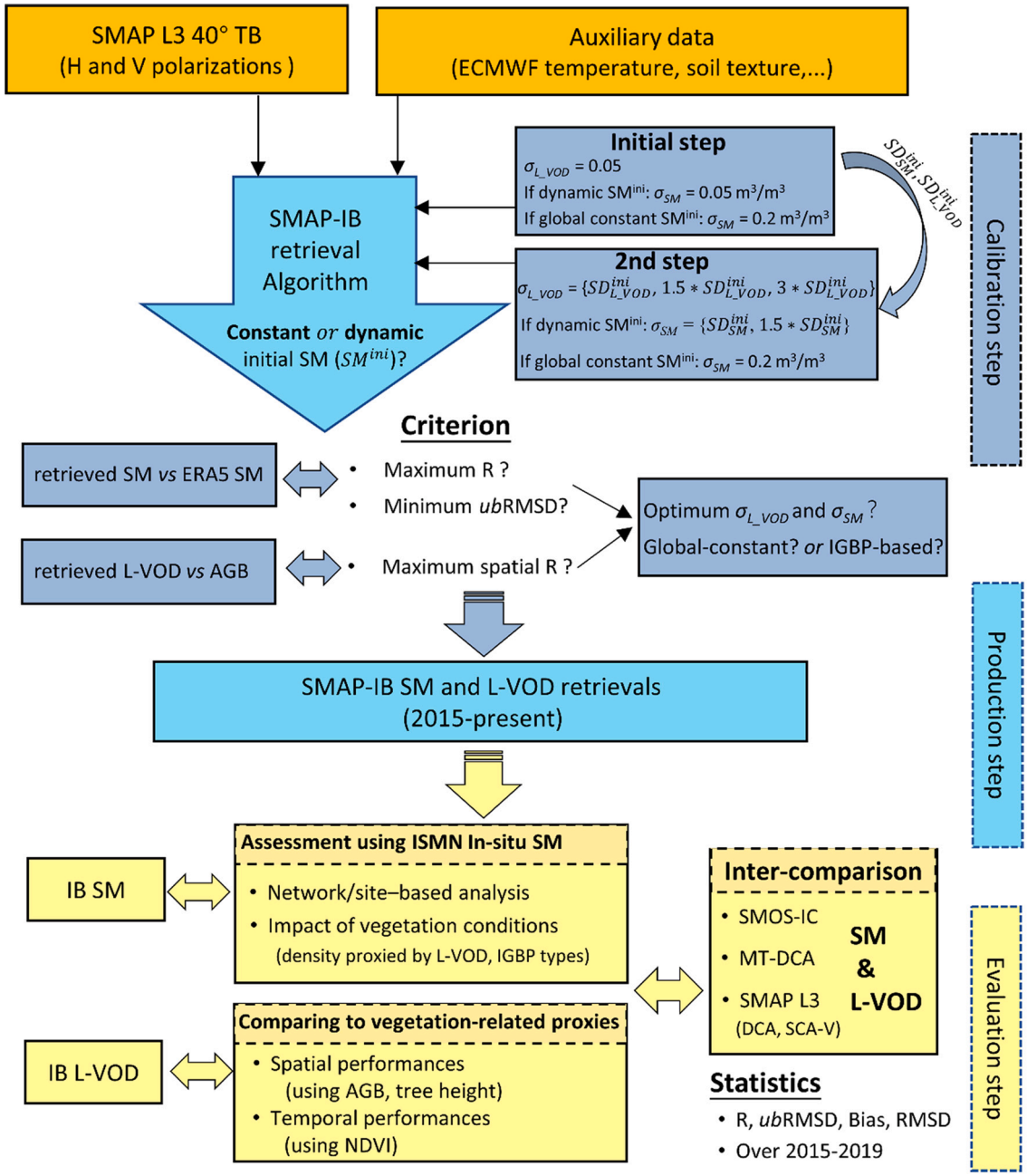

Fig. 2. Flow chart presenting the development and assessment of SMAP-IB: inputs (in orange), parameter (i.e., σ_{SM} and σ_{L_VOD}) calibration (in deep blue), SM and L-VOD production (in light blue), and performance analysis step (in yellow). (For interpretation of the references to colour in this figure legend, the reader is referred to the web version of this article.)

$$LVOD^{ini}(t) = \begin{cases} average\left(LVOD^{*}_{t-1}, LVOD^{*}_{t-2}, \cdots, LVOD^{*}_{t-w}\right) \text{ if available} \\ LVOD_m(t) \text{ if mean LVOD value of previous w days not available} \end{cases}$$

$$SM^{ini}(t) = \begin{cases} average\left(SM^{*}_{t-1}, SM^{*}_{t-2}, \cdots, SM^{*}_{t-w}\right) \text{ if available} \\ SM_m(t) \text{ if mean SM value of previous w days not available} \end{cases} \quad (3)$$

where $L\_VOD_{\mathrm{m}}(t)$ ($SM_{\mathrm{m}}(t)$) is the average monthly L-VOD (SM) value of the month corresponding to date t. $L\_VOD_{\mathrm{m}}(t)$ and $SM_{\mathrm{m}}(t)$ are both 12-element vector containing pixel-based average monthly L-VOD (or SM) values estimated from previous runs based on an iterative process to initialize the inversion (Wigneron et al., 2021). These values are used only if average values of L-VOD (or SM) cannot be computed over the time interval [t-w, t]. This may happen especially in the high-latitude areas where the frozen period limits the number of days where the retrievals can be made.

In SMAP-IB, we set the value of w = 10 days, which is the same as SMOS-IC V2, as a smaller window may not ensure a stable mean value of previous retrievals before date t and a larger window may violate the assumed rate of change of L-VOD (Li et al., 2020c; Wigneron et al., 2021). Note that this value of w is also close to the time window (i.e., one

week) used in the above-mentioned MT algorithms (Kerr et al., 2016; Konings et al., 2017). In this model setup, the two variables σ_{SM} and σ_{L_VOD}, which determine the confidence of (or the distance from) the estimated first guess value of SM^{ini} and L_VOD^{ini}, still need to be optimized in the SMAP-IB algorithm. For this purpose, the two following performance criteria were considered during the parameter optimization:

i) criterion for SM, quality of SMAP-IB SM was evaluated *vs* the global daily ERA5 reanalysis SM dataset;
ii) criterion for L-VOD, quality of SMAP-IB L-VOD was evaluated considering the spatial correlation between time averaged L-VOD and Saatchi AGB;

The optimal estimation of the two variables (σ_{SM} and σ_{L_VOD}) based on these 2 criteria was performed using the four metrics presented later in Section 2.2.3. As in the SMOS-IC V2 algorithm configuration, which sets a global constant value of $\sigma_{L\_VOD} = 0.05$, we initially set both σ_{SM} and σ_{L_VOD} globally equal to 0.05 (e.g., $\sigma_{SM}^{ini} = 0.05$ m^3/m^3 and $\sigma_{L\_VOD}^{ini} = 0.05$). The performance of the SM retrievals under this configuration was better than SMOS-IC V2 in most land cover types (Table S2–5). However, considering that the vegetation water content depends on the vegetation structure (or types) (Li et al., 2021) and there are large spatio-temporal variations in soil moisture (Wigneron et al., 2017), we attempted to improve this result and evaluated other cases corresponding to different pixel-based σ_{SM} and σ_{L_VOD} values. In these cases, σ_{SM} and σ_{L_VOD} were linear multiples of the daily standard deviation (i.e., SD_{SM}^{ini} and $SD_{L\_VOD}^{ini}$) calculated from the SM and L-VOD retrieved from the initial configuration (i.e., $\sigma_{SM}^{ini} = 0.05$ m^3/m^3 and $\sigma_{L\_VOD}^{ini} = 0.05$), and were as follows:

$\sigma_{SM} = \{SD_{SM}^{ini}, 1.5 * SD_{SM}^{ini}\}$;

$\sigma_{L\_VOD} = \{SD_{L\_VOD}^{ini}, 1.5 * SD_{L\_VOD}^{ini}, 3 * SD_{L\_VOD}^{ini}\}$;

Note that the range of the σ_{SM} and σ_{L_VOD} values tested here are relatively narrow, because they have been shortened after some preliminary tests (not shown here to focus on the main results of the calibration step). Moreover, to highlight the effect of using a dynamic initialization of SM, we also tested the results of all σ_{L_VOD} cases corresponding to the use of the same initialization (weakly constrained) of SM as that of the SMOS-IC algorithm, that is, the initial SM value and σ_{SM} are both globally set to 0.2 m^3/m^3. The results obtained for these cases were assessed by comparison to the aforementioned calibration datasets (Saatchi AGB for L-VOD and ERA5 SM for SM).

2.2.3. Metrics used for assessing the SMAP-IB retrievals

The retrievals of SM and L-VOD from SMAP-IB as well as from four other algorithms were evaluated for both SM and L-VOD against, respectively, *in-situ* measurements and vegetation-related proxies (i.e., MODIS NDVI, AGB and tree height), and then, the resulting statistical metrics were inter-compared. For consistency and reliability purposes, the following criteria (or data pre-processing strategies) were adopted: i) to ensure a fair inter-comparison, the evaluation of the SM and L-VOD products was performed for the same period from April 2015 to March 2019 for all products and using observations acquired during the morning overpass at 6:00 am (i.e., ascending for SMOS and descending for SMAP) rather than afternoon because of better thermal equilibrium conditions between the soil and the vegetation canopy (Wigneron et al., 2007; Ma et al., 2019); ii) applying same data filtering to all products for SM values outside of [0, 0.6 m^3/m^3] and L-VOD values outside of [0,2] (Li et al., 2020b); iii) all potentially spurious observations caused by open water fraction, snow coverage, frozen conditions and radio frequency interference (RFI) were filtered using the respective flags of each product. For instance, both the SMAP-IB and SMOS-IC daily retrievals were excluded when the flag of "Scene Flags" > 1 to filter out retrievals impacted by strong topography, pixel heterogeneity (e.g., water and urban fractions) and presence of frozen conditions (e.g., snow, ice); we also used the SMOS-IC filter defined by "TB-RMSE" > 8 K to reduce the impact of strong RFI (Li et al., 2020b; Wigneron et al., 2021). Note that SMAP-IB has the same product attribute layer as SMOS-IC, which is defined in Supplementary data format of Wigneron et al. (2021). For SMAP DCA and SCA-V retrievals, pixels with more than 5% of water fraction or more than 10% of frozen fraction were filtered out. Note that "the recommended value by the retrieval quality flag", a filter criterion often used in previous validation efforts (Al-Yaari et al., 2019; Bai et al., 2019), was only applied to non-forest areas in this study. This was done here as a recent assessment made by the SMAP team shows that SMAP has also a great potential to retrieve SM in forest areas where quality flags are typically triggered as non-recommended (Ayres et al., 2021).

The assessment of the L-VOD retrievals was based on the analysis of the temporal and spatial correlation with vegetation-related proxies as in Li et al. (2021) using the Pearson correlation coefficient (R). The assessment of the SM retrievals was made using four classical statistical metrics including R, Bias (m^3/m^3), RMSD (m^3/m^3; Root Mean Square Difference), and the unbiased RMSD (*ub*RMSD; m^3/m^3), as suggested by Al-Yaari et al. (2019). Among which, the R and *ub*RMSD metrics, which are less impacted than Bias and RMSD by the issue of no 1 to 1 reference SM values available (Entekhabi et al., 2010b; Xing et al., 2021), were regarded as first-order metrics in both the calibration and evaluation steps of this study. Specifically, this consideration was made as the *in-situ* measurements or ECMWF model outputs do not represent the SM values as "observed" by the satellites considering (i) the scale/resolution gap between point-scale *in-situ* observations and grid-scale satellite footprints and (ii) the different "sampling" depths of the *in-situ* or ECMWF modelled SM and satellite-based observations (Wigneron et al., 2021). Moreover, to narrow the time discrepancy between the *in-situ* measurements and the satellite observations, we only considered the *in-situ* SM values matching with the instantaneous overpass of the satellite observations within a time window of 1 h for each product. To get robust statistical results after calculating the metrics between the satellite data and the *in-situ* observations, we also discarded several cases from the analyses: i) sites where the number of data pairs is less than 31 days (~one month) or where non-significant correlations were obtained (*p*-values >0.05); ii) sites where all five SM products obtained R values lower than 0.4 (Ma et al., 2019; Li et al., 2020b). It should be noted that, although the representativeness errors of *in-situ* measurements could affect the absolute values of the metrics (Abowarda et al., 2021; Gruber et al., 2020) and decay the ability to detect differences between the products, the analysis presented here is comparative in nature and tended to provide information on relative pros and cons of each product. Finally, the median of each metric for all sites pertaining to a L-VOD level defined in Table 1 or an IGBP land cover type was calculated (Wigneron et al., 2017, 2021).

3. Results

In this section, we first focused on the calibration of the σ_{SM} and σ_{L_VOD} parameters of the SMAP-IB inversion model. Then, the performance of SMAP-IB for the retrieval of SM and L-VOD was separately assessed through an inter-comparison with four other products (i.e., SMOS-IC V2, SMAP MT-DCA, SMAP DCA and SCA-V).

3.1. Calibration of σ_{SM} and σ_{L_VOD}

Based on the inter-comparison results of the different cases (Table 2 and S2–6), we found that the values of σ_{SM} and σ_{L_VOD} parameters producing the highest temporal correlation values were not very consistent with those producing the lowest *ub*RMSD values especially for different vegetation types when evaluating SMAP-IB retrieved SM against ERA5 modelled SM. However, it was obvious that using the method proposed in this study, that is, applying a dynamic SM value to initialize the inversion, improved results were obtained compared to using a static constant initial SM value. Moreover, it was also found that changing the values of σ_{SM} and σ_{L_VOD} had only a slight impact on the metrics of SMAP-

IB L-VOD in this model setup. Specifically, the spatial correlation between the time averaged L-VOD and Saatchi AGB was globally ~0.88 for all cases. This means that the possible circularity when using the same AGB data in the "calibration" and "assessment" steps of L-VOD is very limited in this study, as the value of different settings has a very low impact on the L-VOD results (Wigneron et al., 2021). In contrast, for the SM retrievals, the calibration step based on model simulations is totally independent of the evaluation step which is based on independent ISMN observations (see Section 3.2). Furthermore, the small performance difference between these test configurations and the initial configuration also demonstrated that the final results of SMAP-IB depend very weakly on the quality of the calibration data.

Combining Table 2 and S2–6, it can be seen that for a given value of σ_{SM}, ${\sigma_{L\_VOD}}^{IB} = 3 * {SD_{L\_VOD}}^{ini}$ is the optimum σ_{L_VOD} value in terms of both temporal correlation and *ub*RMSD for non-forest areas, while ${\sigma_{L\_VOD}}^{IB} = {SD_{L\_VOD}}^{ini}$ is the optimum value for forest areas. Therefore, we tested another set of combined σ_{L_VOD}, namely ${\sigma_{L\_VOD}}^{IB} = 3 * {SD_{L\_VOD}}^{ini}$ for non-forest areas and ${\sigma_{L\_VOD}}^{IB} = {SD_{L\_VOD}}^{ini}$ for forest areas. For this combined and optimum σ_{L_VOD} setting, best scores in terms of both temporal correlation and lowest *ub*RMSD were obtained for ${\sigma_{SM}}^{IB} = {SD_{SM}}^{ini}$. This latter value was selected for the SMAP-IB algorithm.

3.2. Soil moisture retrievals

3.2.1. Global spatial patterns and temporal dynamics

At a global scale, SMAP-IB SM retrievals presented similar spatial patterns as SMAP DCA and SCA-V, with lowest SM values over the arid and semi-arid areas (e.g., Sahara, Australia and desert areas in central Asia) and highest SM values in tropical rainforests (Fig. 3e, g, i). The same patterns could generally be observed in SMOS-IC and MT-DCA but with drier values, especially over densely vegetated areas (Fig. 3a, c). There are a few exceptions and notably the SMAP-IB SM retrievals in the Appalachian region of the eastern US were almost as wet as in the intact forests of South America, while other SM products showed a gradient between these two regions. In addition, the obvious dry-wet gradient between the tropical intact forests and non-forest areas found with SMAP-IB, SCA-V, and DCA was not well reflected in SMOS-IC and MT-DCA. More surprisingly, MT-DCA had an inverse dry-wet gradient between the Amazon rainforests and the southeastern Brazil and Uruguay compared to the four other SM products, which was also evidenced in Konings et al. (2017). In terms of absolute SM values, DCA exhibited higher SM values than SMAP-IB and SCA-V over most of the globe, except for high latitudes (above ~60°N), where the SM values of SMAP-IB were the highest. Conversely, SMAP-IB was more humid than SCA-V in tropical intact forests and southeastern China (Fig. 3g, i).

To further analyze the dynamics of the different SM products, the mean annual seasonal amplitude (SA) was calculated, as shown in the second column of Fig. 3. The seasonal amplitude is the difference between the peak defined by the 95% percentile and the trough defined by the 5% percentile of the SM time-series after applying a 45-day sliding-average window to the data (Konings et al., 2017). Regarding the distribution of SA, analogous spatial patterns could generally be found among SMAP-IB, SCA-V, DCA and SMOS-IC. For example, all datasets had relatively high SA values in western Russia, Sahel, Miombo woodlands and Indochina, while the SA values of MT-DCA were globally higher, even for the dense forest areas of the Amazon and Congo basins and the southwestern US regions, which were known to be relatively drier than the eastern US regions (Sheffield et al., 2004). In terms of absolute values of SA, the SMAP-IB SM retrievals presented generally lower values compared to DCA and MT-DCA, but similar to SCA-V and SMOS-IC in the tropical forest areas. The Hovmöller diagrams showing the monthly mean SM values per latitude (Hovmöller, 1949; Al-Yaari et al., 2014) confirmed some of the above results (Fig. S1). It can be viewed that SMAP-IB SM had generally common periodical features with the four other SM products in terms of time and latitude. For instance, all the five SM products showed a distinct seasonal pattern in the Southern Hemisphere (> 35°S) and all of them could well detect the meridional shift of the Intertropical Convergence Zone (ITCZ), but SMAP-IB, DCA and SCA-V showed changes with a higher seasonal cycle, as found in the MERRA-Land modelled soil moisture (Al-Yaari et al.,

Table 2
Calibration of σ_{SM} and σ_{L_VOD}: the results obtained for these cases were assessed by comparison to the calibration datasets (Saatchi AGB for L-VOD and ERA5 SM for SM).

SM initialization type	Configurations		Retrieved SM *vs* ERA5 SM				Retrieved L-VOD *vs* Saatchi AGB
	σ_{L_VOD}	σ_{SM} (m^3/m^3)	Temporal R	*ub*RMSD(m^3/m^3)	Bias (m^3/m^3)	RMSD(m^3/m^3)	Spatial R
Dynamic SM^{ini} (Eq. (3))	0.05	0.05	0.73	0.046	−0.061	0.094	0.89
	${SD_{L\_VOD}}^{ini}$	${SD_{SM}}^{ini}$	0.73	0.048	−0.057	0.095	0.89
	${SD_{L\_VOD}}^{ini}$	1.5 * ${SD_{SM}}^{ini}$	0.73	0.051	−0.055	0.096	0.89
	1.5 * ${SD_{L\_VOD}}^{ini}$	${SD_{SM}}^{ini}$	0.74	0.047	−0.054	0.094	0.88
	1.5 * ${SD_{L\_VOD}}^{ini}$	1.5 * ${SD_{SM}}^{ini}$	0.73	0.050	−0.051	0.095	0.88
	3 * ${SD_{L\_VOD}}^{ini}$	${SD_{SM}}^{ini}$	0.74	0.046	−0.050	0.093	0.88
	3 * ${SD_{L\_VOD}}^{ini}$	1.5 * ${SD_{SM}}^{ini}$	0.74	0.049	−0.047	0.094	0.88
	non-forest area: 3 * ${SD_{L\_VOD}}^{ini}$ forest area: ${SD_{L\_VOD}}^{ini}$	**${SD_{SM}}^{ini}$**	**0.74**	**0.046**	**−0.054**	**0.093**	**0.88**
	non-forest area: 3 * ${SD_{L\_VOD}}^{ini}$ forest area: ${SD_{L\_VOD}}^{ini}$	1.5 * ${SD_{SM}}^{ini}$	0.74	0.049	−0.052	0.094	0.88
Global constant SM^{ini} ($SM^{ini} = 0.2$ m^3/m^3)	0.05	0.2	0.72	0.052	−0.074	0.100	0.86
	${SD_{L\_VOD}}^{ini}$	0.2	0.71	0.053	−0.072	0.099	0.87
	1.5 * ${SD_{L\_VOD}}^{ini}$	0.2	0.72	0.051	−0.070	0.097	0.86
	3 * ${SD_{L\_VOD}}^{ini}$	0.2	0.73	0.049	−0.067	0.094	0.85
	non-forest area: 3 * ${SD_{L\_VOD}}^{ini}$ forest area: ${SD_{L\_VOD}}^{ini}$	0.2	0.72	0.051	−0.070	0.097	0.86
SMOS-IC ($SM^{ini} = 0.2$ m^3/m^3)	0.05	0.2	0.69	0.052	−0.107	0.126	0.88

Note: ${SD_{L\_VOD}}^{ini}$ or ${SD_{SM}}^{ini}$ is the daily standard deviation of L-VOD or SM calculated from the retrieval results of the initial configuration (i.e., ${\sigma_{L\_VOD}}^{ini} = 0.05$ and ${\sigma_{SM}}^{ini} = 0.05$ m^3/m^3). The configuration bolded in the table represents the selected setting for the SMAP-IB retrieval algorithm.

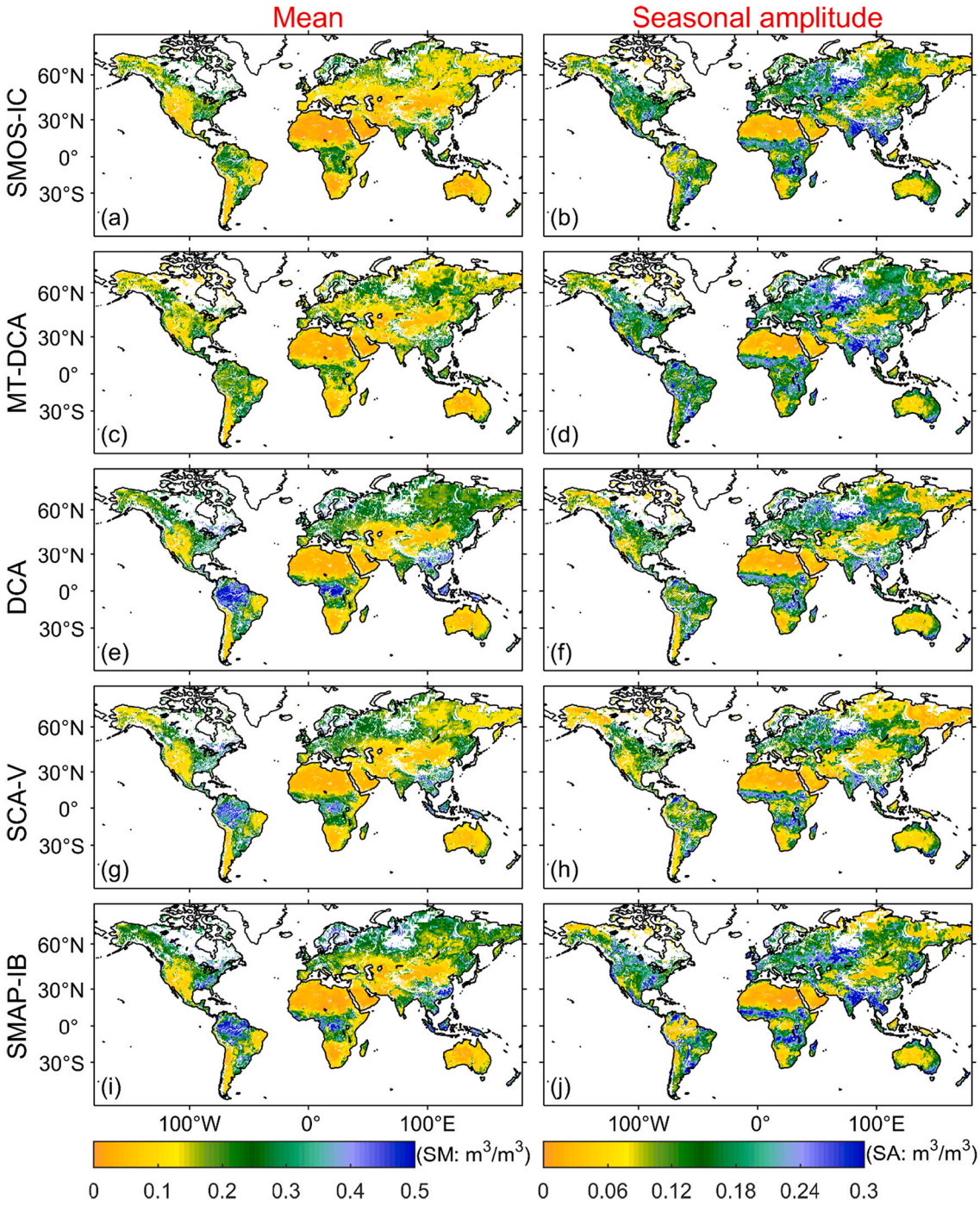

Fig. 3. Global distribution of time averaged and mean annual seasonal amplitude (SA) of the different SM products from April 2015 to March 2019 for a-b) SMOS-IC, c-d) MT-DCA, e-f) DCA, g-h) SCA-V and i-j) SMAP-IB. Note that the seasonal cycle is defined by applying a 45-day moving window filter to the data when calculating the seasonal amplitude.

2014).

3.2.2. *Network-based validations*

The statistics of the validation results of the five SM products against the *in-situ* measurements are shown in Table 3, except RMSD (Table S7). In the table, as performed in previous evaluation studies (Al-Yaari et al., 2019; Li et al., 2020b), the median values of all metrics (i.e., R, *ub*RMSD and Bias) were calculated for each ISMN network used in this study. In terms of temporal variations of *in-situ* SM, SMAP-IB presented the highest overall median R value of 0.74, followed by MT-DCA ($R = 0.71$), which was slightly better than SCA-V, DCA and SMOS-IC with the same R value of 0.69 ("All" item in last rows of Table 3). To be noted, among these networks, SMAP-IB obtained the highest R values of all the five SM products over most of the networks (15 over 19). Regarding the different networks, it can be seen that the overall best R value for all the five SM products was obtained over the SOILSCAPE network. In contrast, the lowest correlations for SMAP-IB, DCA, SCA-V were found for the RSMN network, while the lowest ones for MT-DCA and SMOS-IC were obtained for the MySMNet network ($R < 0.6$). In terms of characterizing the absolute value of *in-situ* SM, DCA performed best compared to the four other SM products, with a lowest median *ub*RMSD value of 0.056 m^3/m^3. Interestingly, in line with the recent validation work of Ayres et al.

(2021) and Colliander et al. (2021), DCA yielded similar (or even the best) scores to (than that of) SCA-V over most of the networks, which confirms the quality of the new version of the modified DCA.

Very close to DCA, SCA-V and SMAP-IB had similar performances in terms of *ub*RMSD, with values of 0.058 m^3/m^3 and 0.059 m^3/m^3, respectively. The *ub*RMSD values obtained by SMAP-based products were all lower than 0.060 m^3/m^3, except for MT-DCA with a median value of 0.063 m^3/m^3. Regarding the different networks, the best and poorest values obtained by the different products were not consistent, although it is noted that some networks may include a low number of SM stations and cover fewer footprint pixels (Table 1). For instance, the lowest *ub*RMSD values of SMAP-IB and SMOS-IC were obtained over DAHRA, while those of MT-DCA and DCA were obtained over AMMA-CATCH and SCA-V over NGARI. Among these networks, DCA obtained the highest performances in terms of *ub*RMSD over most of the networks (10 over 19), followed by SMAP-IB with 5 networks and SCA-V with 4. We also noted that SMAP-IB presented lower *ub*RMSD values than MT-DCA in almost all networks, except for AMMA-CATCH, NAQU, SOILSCAPE and TERENO. Regarding Bias, both SMAP-IB and SCA-V obtained best results, with very small bias values of 0.002 m^3/m^3 and 0.008 m^3/m^3. They were followed by MT-DCA (small underestimation) and DCA (small overestimation) with a similar absolute bias value of ~0.013 m^3/m^3. Different from the previous evaluation efforts (Al-Yaari et al., 2019; Ma et al., 2019), which found that the SMAP products are generally drier than the ISMN observations, we found here that the new version of SMAP SCA-V and DCA products are wetter than the ground observations in most networks. But consistent with previous evaluations, the new version of SMOS-IC (V2) still obtained a higher bias value, with a median value of −0.054 m^3/m^3. It should be noted that a supplementary evaluation considering only dense observation footprints defined as 36 km footprint cells comprising a number of ground stations >3, especially for bias (Table S7), is consistent with the inter-comparison results obtained above.

As an alternate way to visualize the performance of each product at the site scale, Fig. 4 illustrates the time series of the five SM products at two *in-situ* sites with low (SCAN) and moderate (SMOSMANIA) vegetation coverage. It can be seen that in both sites, the SM estimates of SMAP-IB, like the other four products, tracked quite well the dry-down trends of the *in-situ* measurements.

3.2.3. Assessment based on different vegetation conditions

To ease the inter-comparison between the different SM products, a map illustrating which SM products had the best scores in terms of per-site temporal correlation and *ub*RMSD against the *in-situ* measurements is provided in Fig. 5. Note that the number of sites with the best performance for each product was also counted, as shown in the brackets after the product name in Fig. 5. In general, SMAP-IB presented the highest R values with the *in-situ* observations over more than one-half (234) of the sites, which were mainly distributed in the mid-western US covered by grasslands and mid-eastern US covered by croplands, while the highest R values in the central and southeast coastal regions of the US were obtained from other SMAP algorithm products, e.g., DCA, SCA-V and MT-DCA. Here, consistent with Table 3, it once again confirmed the ability of SMAP-IB to capture temporal trends of *in-situ* SM, as R is generally considered to be the most important indicator in quantifying the skills of satellite-based SM, especially when a large number of sparse observation networks are used (Zeng et al., 2020; Ma et al., 2019). In terms of *ub*RMSD, while the five products had comparable performance at 138 sites, SCA-V demonstrated the best performance over 78 sites mainly distributed in US and southeastern Europe, followed very closely by SMAP-IB (74) and DCA (72). However, unlike SCA-V and DCA, which were evenly distributed throughout the US, the best performing sites of SMAP-IB were mainly concentrated in the northeastern US. It was generally found from Fig. 5 that SMAP-based products presented better scores than SMOS-based products especially in Europe and Asia, which may be due to the fact SMOS is more affected by RFI in these areas than elsewhere and is consistent with the validation conducted by Al-Yaari et al. (2019).

To further shed light on the effects of vegetation density on the SM estimates among the different products, the gauge-based error metrics were stratified based on different L-VOD levels obtained from SMOS-IC (Fig. 6). Regarding the temporal correlation (R) metric (the first row of Fig. 6), it was found that all the five SM products presented a relatively low sensitivity to the vegetation effects directly parameterized by L-VOD here, as their R values did not show a decreasing trend as the L-VOD value increases. On the contrary, the R values with the *in-situ* measurements were even higher in middle-level VODs (e.g., VOD-IV and VOD-V) than low-level VODs (e.g., VOD-II). In particular, all SM products had the highest R values for the VOD-V range by exhibiting a median R value above 0.71, except for SMAP-IB, which achieved the

Table 3
The network-based statistical validation results of SMOS-IC, MT-DCA, DCA, SCA-V and SMAP-IB against ISMN *in-situ* measurements for April 2015–March 2019. Best performance of the five SM products in each network is typeset in boldface.

Metrics	R($p < 0.05$)					*ub*RMSD(m^3/m^3)					Bias(m^3/m^3)				
Networks	SMOS-IC	MT-DCA	DCA	SCA-V	SMAP-IB	SMOS-IC	MT-DCA	DCA	SCA-V	SMAP-IB	SMOS-IC	MT-DCA	DCA	SCA-V	SMAP-IB
SCAN	0.70	0.72	0.69	0.69	**0.74**	0.056	0.059	**0.050**	**0.050**	0.054	−0.048	−0.025	0.009	**0.005**	0.007
SNOTEL	0.61	0.67	0.65	0.63	**0.72**	0.073	0.076	0.067	**0.066**	**0.066**	−0.073	−0.016	**−0.002**	−0.013	−0.018
AMMA-CATCH	0.86	0.90	0.89	0.88	**0.91**	0.033	0.033	**0.031**	0.035	0.035	**0.015**	0.027	0.036	0.047	0.035
DAHRA	**0.79**	0.74	0.77	0.66	0.75	**0.023**	0.040	0.032	0.050	0.029	−0.019	**−0.001**	0.006	0.020	−0.009
FR_Aqui	0.60	0.67	0.63	0.62	**0.85**	0.069	0.071	0.076	0.071	**0.054**	**0.013**	0.073	0.084	0.086	0.132
HOAL	0.57	0.68	0.69	0.67	**0.79**	0.047	0.045	0.047	0.047	**0.038**	−0.174	−0.121	−0.025	**−0.005**	−0.012
MAQU	**0.73**	0.65	0.65	0.62	0.66	**0.063**	0.065	0.070	0.074	**0.063**	**−0.018**	−0.099	0.064	0.043	0.093
NAQU	0.78	0.86	0.86	**0.87**	0.86	0.065	0.041	**0.037**	0.086	0.057	0.070	−0.026	**0.016**	0.139	0.107
NGARI	0.74	0.68	0.65	0.65	**0.78**	0.030	0.043	0.038	**0.026**	0.032	−0.056	−0.027	**0.011**	−0.017	−0.013
RISMA	0.66	0.61	**0.69**	**0.69**	0.68	0.059	0.068	**0.051**	0.052	0.061	−0.088	−0.088	−0.018	**0.012**	−0.030
SMOSMANIA	0.76	0.75	0.78	0.78	**0.80**	0.053	0.061	0.055	**0.050**	0.054	−0.133	−0.010	**−0.006**	−0.010	−0.029
SOILSCAPE	0.91	**0.93**	0.92	0.92	**0.93**	0.050	0.061	**0.036**	0.037	0.086	−0.029	0.049	0.030	**0.014**	0.068
TERENO	0.79	0.79	0.76	0.74	**0.80**	0.046	0.044	**0.042**	0.045	0.047	−0.179	−0.146	−0.036	**−0.023**	−0.085
USCRN	0.73	0.72	0.70	0.72	**0.77**	0.051	0.054	**0.048**	0.049	0.052	−0.049	−0.018	0.013	**0.008**	**0.008**
HOBE	0.67	0.70	0.67	0.65	**0.76**	**0.050**	0.056	0.058	0.055	0.053	−0.026	−0.046	0.050	0.047	**0.002**
MySMNet	0.42	0.56	0.63	0.63	**0.70**	0.072	0.040	0.046	0.048	**0.034**	0.169	**0.066**	0.241	0.261	0.170
OZNET	0.79	0.80	0.81	0.77	**0.82**	0.062	0.073	**0.058**	0.063	0.070	**0.003**	0.034	0.053	0.052	0.031
REMEDHUS	0.79	0.78	0.80	0.79	**0.82**	0.043	0.049	**0.038**	0.040	0.046	−0.031	0.031	0.011	**0.007**	0.010
RSMN	0.60	0.62	0.57	0.58	**0.65**	0.072	0.070	**0.056**	0.058	0.070	**0.008**	0.025	0.095	0.089	0.048
All	0.69	0.71	0.69	0.69	**0.74**	0.060	0.063	**0.056**	0.058	0.059	−0.054	−0.013	0.014	0.008	**0.002**

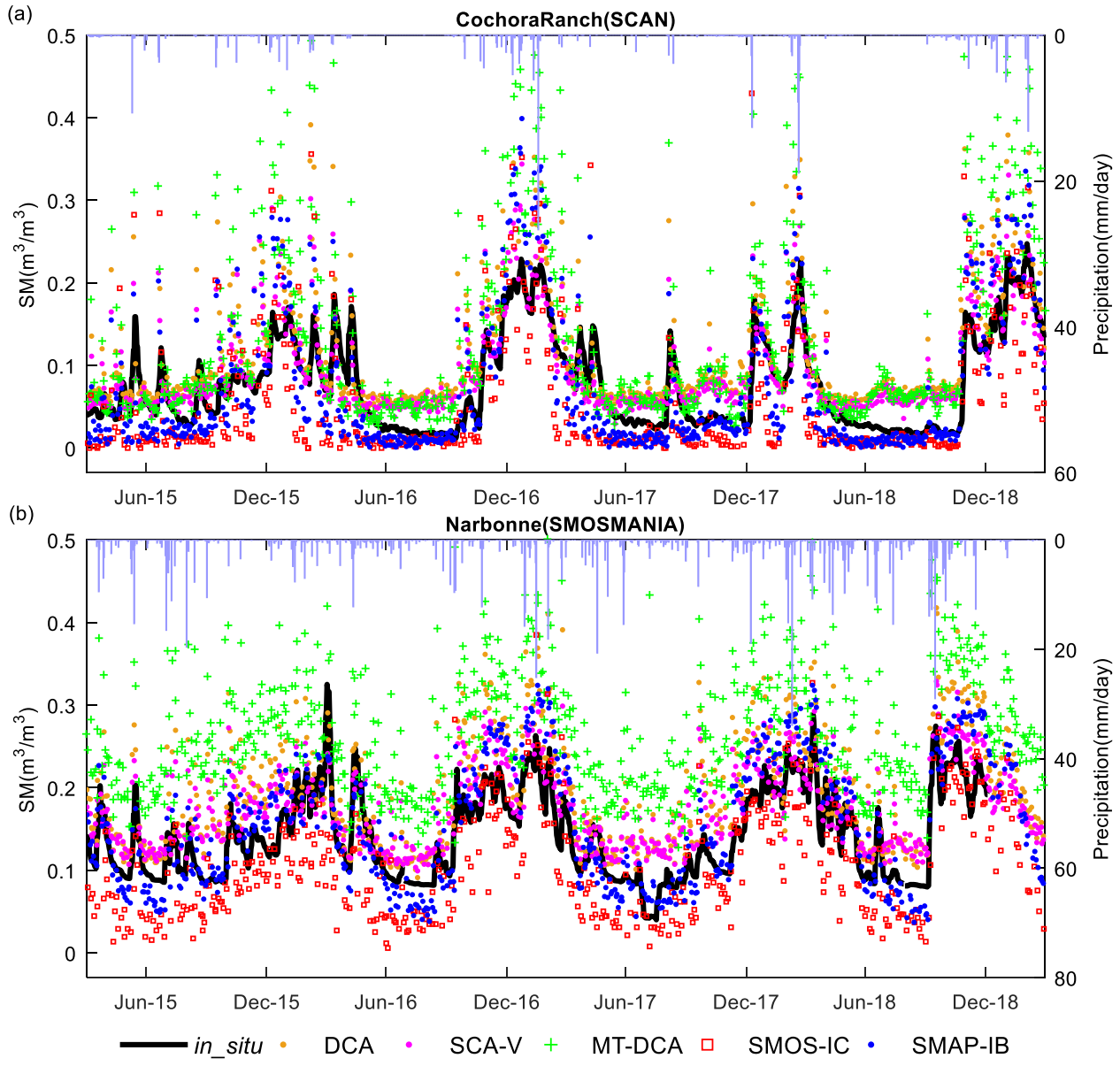

Fig. 4. Time series of the five SM products between April 2015 and March 2019 at a) CochoraRanch; and b) Narbonne, from the SCAN and SMOSMANIA networks, respectively. Each plot also contains daily precipitation (mm/day) shown in axis on the right side (light blue bar). Note that a 7-day moving window filter was applied to the *in-situ* observations to distinguish them from the satellite-based SM. (For interpretation of the references to colour in this figure legend, the reader is referred to the web version of this article.)

highest R value of 0.77 in VOD-III. In general, SMAP-IB presented higher R values than the other SM products in all VOD intervals, especially for VOD conditions from 0 to 0.4, while similar performances between the four other SM products (MT-DCA, DCA, SCA-V and SMOS-IC) could be found from VOD-III to VOD-V. A relatively large difference between DCA (lower performance) and the other three products was found in VOD-I, where MT-DCA performed slightly better, followed by SCA-V and SMOS-IC. Leaving this category aside, it was interesting to find that the new versions of DCA and SCA-V had comparable performance in all the other VOD conditions, consistent with the overall results in Table 3.

In terms of bias, all the five SM products overestimated the *in-situ* measurements in VOD-VI, especially for DCA, showing a highest bias value of 0.15 m^3/m^3, while SMOS-IC generally underestimated the *in-situ* measurements in the other VOD categories particularly for VOD-II, VOD-III and VOD-IV. Considering the *ub*RMSD and RMSD metrics, it was found that all the five SM products presented a relatively high sensitivity to the vegetation effects, as these metric values increased slowly with the increase of L-VOD value (Fig. 6). The newly updated DCA was generally found to have the best performance in all VOD categories, except for category VOD-V, where its *ub*RMSD value (0.066 m^3/m^3) was slightly higher than the four other products. Overall, in terms of *ub*RMSD, SMAP-IB had comparable performance to SCA-V and SMOS-IC in most VOD categories, and the three of them were slightly better than MT-DCA.

Fig. 7 shows the impact of the vegetation types on the performance of the different SM products. Regarding correlation, SMAP-IB correlated better with the *in-situ* observations over most of the vegetation types, except for woody savannas, where DCA and SCA-V ranked the top, with the highest R value of 0.85. Similar skills between the four other products (MT-DCA, DCA, SCA-V and SMOS-IC) were generally found over the forest types, croplands and cropland/natural vegetation mosaics. By exhibiting the lowest R value of 0.57, a larger difference between DCA

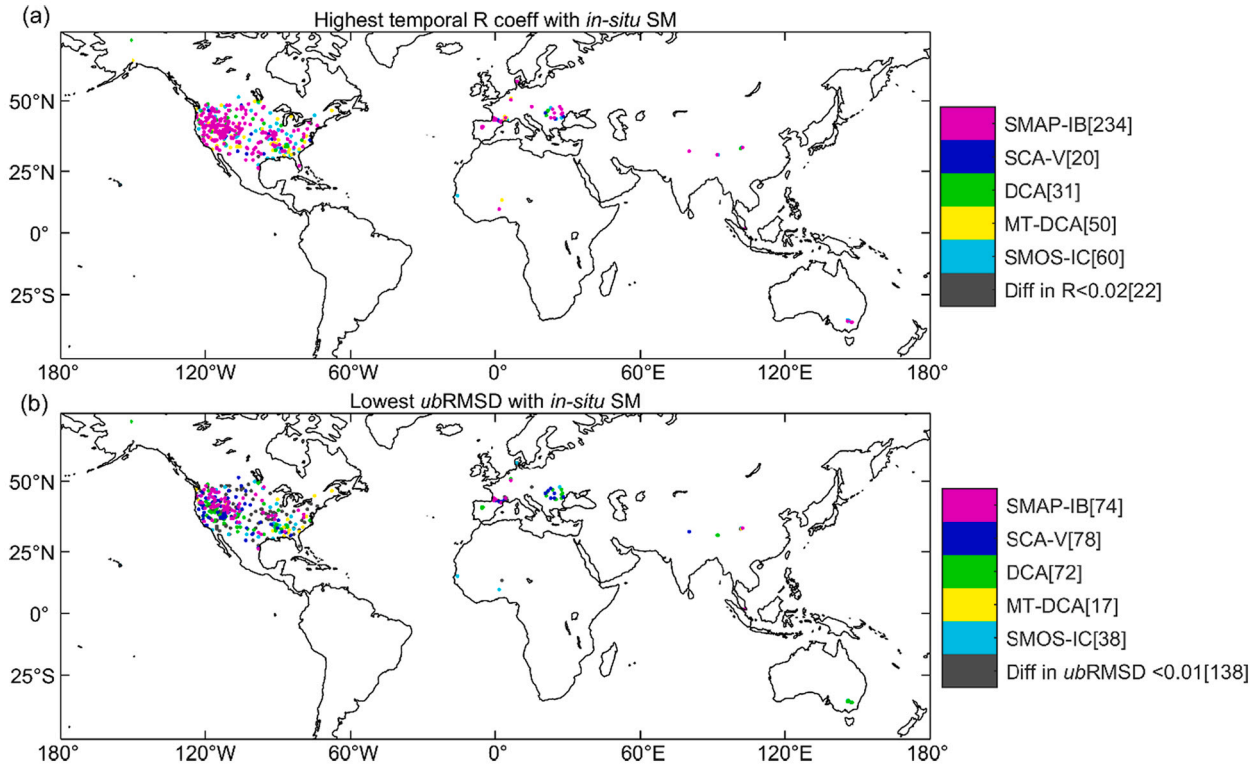

Fig. 5. Maps showing the SM products presenting the best performance with *in-situ* measurements for a) R and b) *ub*RMSD for each site. Note: the sites for which the difference in R (*ub*RMSD) is lower than 0.02 (0.01 m^3/m^3) are indicated by a black colour.

and the other three products was found over shrublands. Interestingly, DCA and SCA-V, which were usually triggered as non-recommended values in forest areas, had performances over forests which were comparable to some low vegetation types (e.g., mixed forests *vs* croplands), which confirmed the latest conclusions of the evaluation of SMAP products in forest areas (Ayres et al., 2021). In terms of *ub*RMSD, SMAP-IB, while presenting the poorest performance over woody savannas, performed similarly to SCA-V over most of the other vegetation types. All five products were found to have the largest bias over the forest types, e.g., DCA over evergreen needleleaf forest with a bias value of 0.092 m^3/m^3, and over deciduous broadleaf forest for all the other products (absolute bias >0.070 m^3/m^3). SMAP-IB agreed well with DCA and SCA-V in terms of the sign of bias in most vegetation types, for instance, they presented overestimations over forest types, and underestimation over grasslands.

3.3. Vegetation optical depth retrievals

3.3.1. Global spatial patterns and temporal dynamics

Fig. 8 shows the global maps of time averaged L-VOD retrievals from SMAP-IB and the four other products from April 2015 to March 2019. Similar spatial patterns were generally found for the five L-VOD products, except for the high latitudes in the Northern Hemisphere, where the L-VOD distribution of SMAP-IB, MT-DCA and SMOS-IC did not show a markedly decreasing gradient starting from ~60°N contrary to DCA and SCA-V, and the spatial patterns of the latter two were very close (Fig. 8g, j). It should be noted that, unlike the latter two, the algorithm of the first three products were independent of the optical vegetation index, that is, no *a priori* information from MODIS NDVI was used to initialize (DCA) or directly estimate L-VOD (SCA-V). Considering the magnitude of L-VOD, MT-DCA presented a higher L-VOD value than DCA, SMAP-IB and SMOS-IC over most of the globe (e.g., tropical forests, western US, Alaska forests and east Siberian taiga), except for eastern US, western and central Europe, where the L-VOD value of DCA was the highest.

In addition to calculating the seasonal amplitude (SA) of the five L-VOD products in a similar way to Fig. 3, we also computed the high-frequency variations in their L-VOD time series though mapping their standard deviation (SD_{hf}) after removing the seasonal trend (Fig. 8). Regarding SD_{hf}, since SCA-V was estimated based on NDVI climatological data, its L-VOD globally presented low high-frequency variations. Similar spatial distribution patterns of SD_{hf} and SA were generally found between SMAP-IB, SMOS-IC, DCA, and SCA-V, all showing relatively high SD_{hf} and SA over Mexico, eastern Brazil, Sahel, eastern Australia, India and boreal forests of Russia, where annual rainfall in most of these regions controlled the vegetation production. In contrast, MT-DCA presented highest SD_{hf} and SA values over the tropical forests (e.g., Amazon and Congo basins). Similar to the findings obtained for SM in Fig. 3, the magnitude of SA and SD_{hf} of L-VOD obtained from MT-DCA were also globally higher than the four other L-VOD products, except for high latitudes (above ~60°N), where the SA and SD_{hf} values of SMAP-IB L-VOD were the highest. The spatio-temporal variations of L-VOD for the five products, summarized using Hovmöller diagrams (monthly mean L-VOD averaged along the longitude range by latitude bands), directly reflected some of the above findings (Fig. S2). In addition, a notable difference between DCA, SCA-V and the three other L-VOD products was found over the northern hemisphere (> 45°N), where the latter exhibited obvious seasonal patterns with higher L-VOD values over the summer corresponding to the period of maximum leaf production and vegetation growth, while this signature was not obvious for DCA and SCA-V.

3.3.2. Spatial performances of the different L-VOD products

Fig. 9 illustrates the density plots of the five L-VOD products with respect to AGB, canopy height and NDVI. Some common features could be found among these five products: they all presented the highest spatial R value when compared to the forest canopy height, while they presented the lowest R value when compared to NDVI, although with

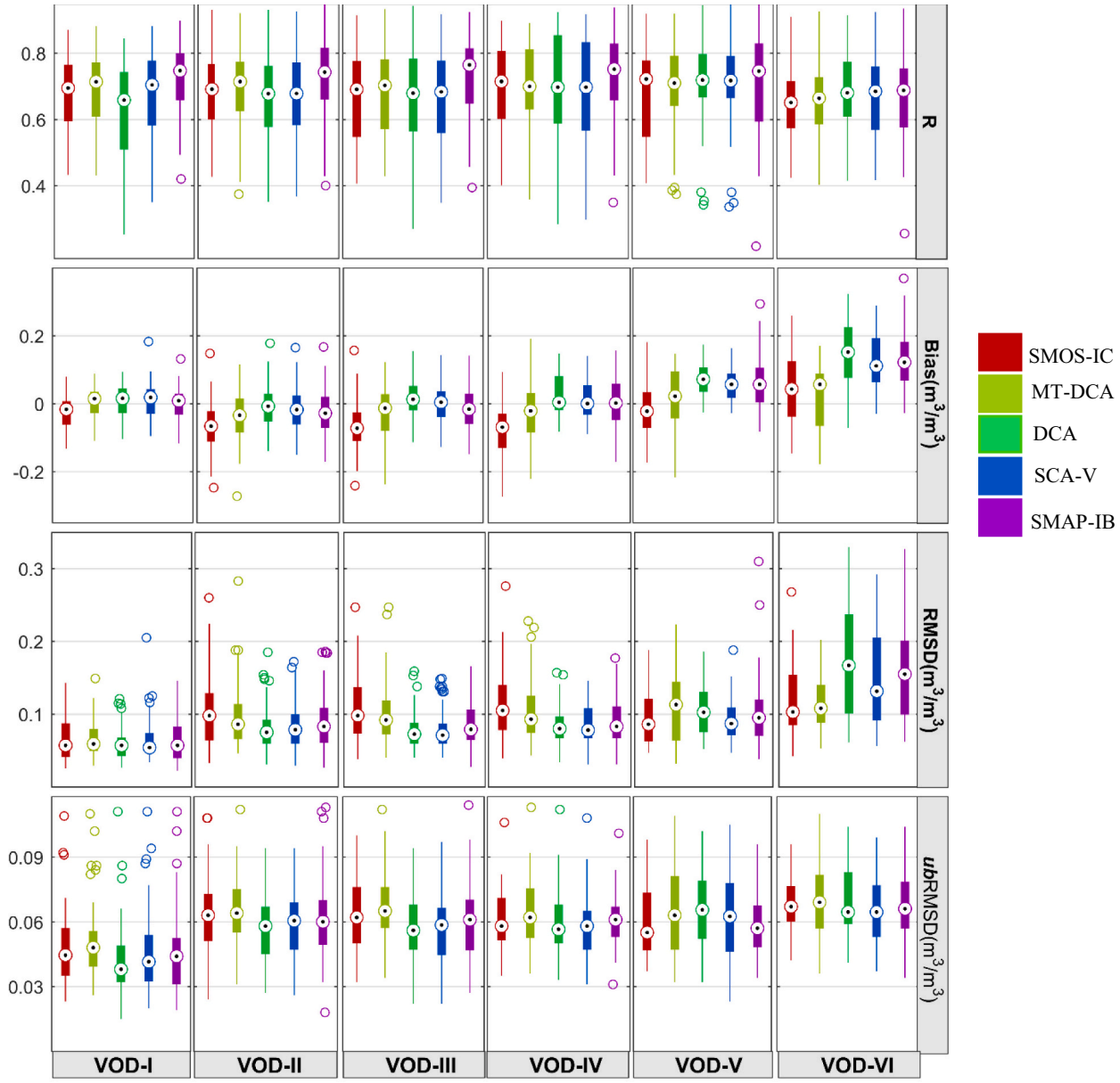

Fig. 6. Boxplot of metrics (R, Bias (m^3/m^3), RMSD (m^3/m^3), and *ub*RMSD (m^3/m^3)) stratified by different L-VOD levels for SMOS-IC, MT-DCA, DCA, SCA-V and SMAP-IB across all ISMN sites during the period of April 2015–March 2019: VOD-I ($n = 52$ sites/pixels); VOD-II ($n = 130$ sites/pixels); VOD-III ($n = 97$ sites/pixels); VOD-IV ($n = 60$ sites/pixels); VOD-V ($n = 37$ sites/pixels); VOD-VI ($n = 41$ sites/pixels). The center dot mark in each box indicates the median value, and the top and bottom edges indicate the 25th and 75th percentiles.

large differences depending on the product. This is due to the fact L-VOD is sensitive to the whole vegetation layer including the woody components, while NDVI is more sensitive to the features of the upper green canopy layer. Most of the L-VOD products had a very good linear relationship with tree height, even for tall forests (height > 20 m), which is in line with the VOD evaluation work conducted by Rodríguez-Fernández et al. (2018) and Li et al. (2021). Fig. 9 also demonstrated that there is a non-linear relationship between L-VOD and AGB, and the obtained R values with the different products were very close (differences by only 0.02 from 0.87 to 0.89). Moreover, most of the L-VOD products could predict well the spatial gradients of AGB, with a correlation value R of ~0.92 calculated between predicted and observed AGB (first column of Fig. 9). Similar results were obtained when comparing L-VOD with tree height: MT-DCA and SMAP-IB presented the highest R with a value of 0.91, while SCA-V had a close value of 0.89.

Some notable differences between the five products could also be found in terms of density distribution (Fig. 9). For instance, the density of the higher L-VOD values (> 1.2) obtained with MT-DCA was higher than the one obtained with the four other L-VOD products at the global scale, which is consistent with Fig. 8. Conversely, DCA and SCA-V L-VOD exhibited obvious saturation effects when AGB ~ 250 Mg ha^{-1} (L-VOD ~ 1.2). In addition, several unevenly concentrated bands could be found for DCA and SCA-V (Fig. 9g,j), which was not the case for SMOS-IC, MT-DCA and SMAP-IB. On the contrary, the latter three presented a smooth relationship with AGB, and there was no strong sign of saturation, which is consistent with the evaluation of several SMOS L-VOD datasets (Rodríguez-Fernández et al., 2018; Mialon et al., 2020). However, the density distribution shapes obtained with them showed a certain degree of distortion when L-VOD is in the range of [0.6, 0.9], corresponding to a range of [200, 300 Mg ha^{-1}] for AGB. The inter-comparison with the global tree height (second column of Fig. 9) confirmed the results presented above. It can be seen that both DCA and SCA-V had high density

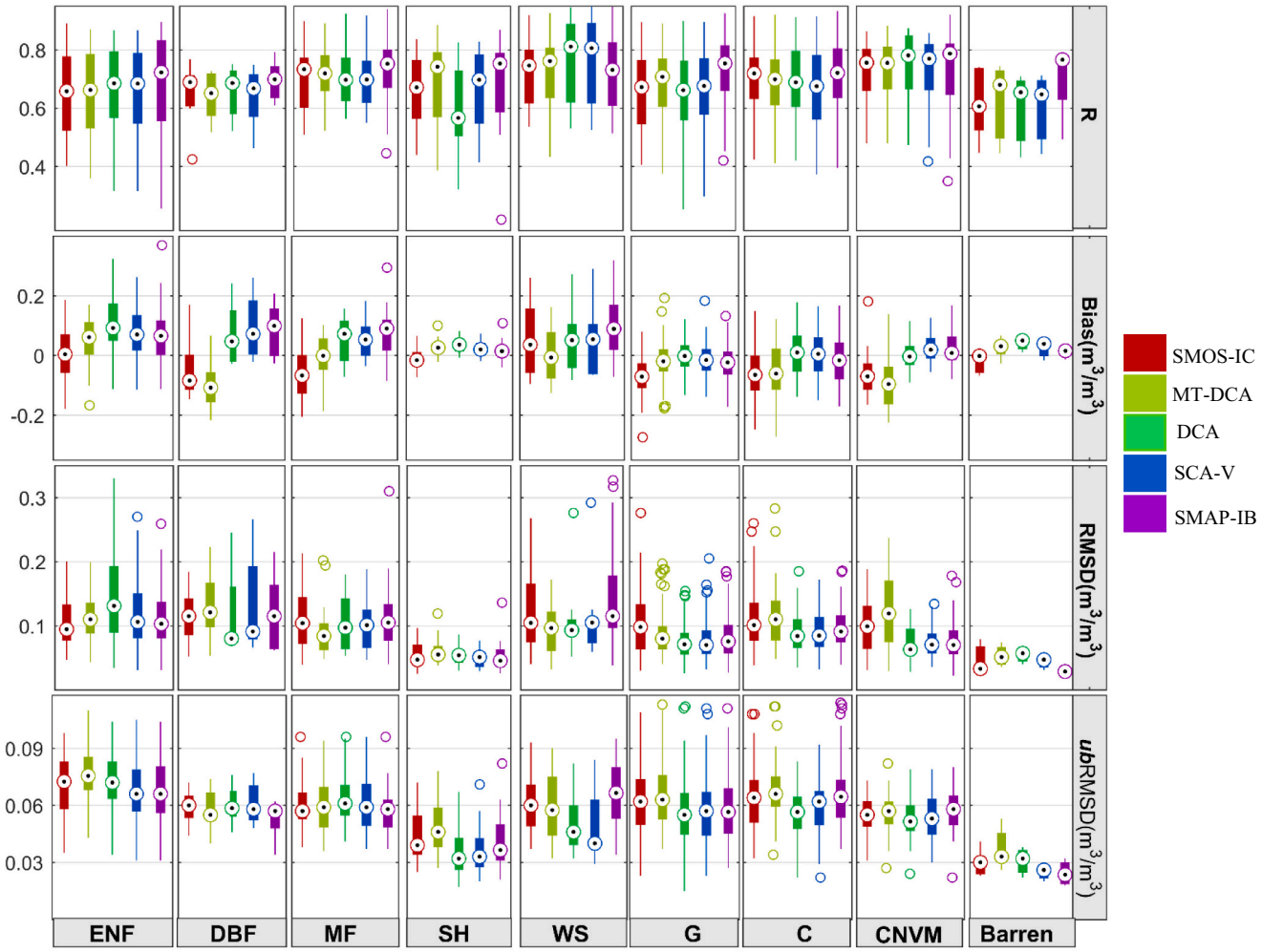

Fig. 7. Same as Fig. 6 except here stratified by different IGBP vegetation types: ENF (n = 48 sites/pixels); DBF (n = 9 sites/pixels); MF (n = 21 sites/pixels); SH (n = 23 sites/pixels); WS (n = 24 sites/pixels); G (n = 177 sites/pixels); C (n = 77 sites/pixels); CNVM (n = 33 sites/pixels); Barren (n = 5 sites/pixels).

concentration and saturation around L-VOD ~ 1.2 and tree height ~ 28 m, and there were even a large number of L-VOD values distributed around ~0 when the tree height reaches 8–16 m, while the three other products showed a good linearity with tree height. In contrast, when compared with NDVI, both DCA and SCA-V L-VOD were less scattered than the other three products. Similar dispersion and distribution shapes between DCA and SCA-V L-VOD (Fig. 9g-l) demonstrated that the new version of DCA initialized with the NDVI climatology may integrate optical information from the latter.

3.3.3. *Temporal performances of the different L-VOD products*

As the L-VOD obtained with DCA and SCA-V both contain NDVI information and to avoid circularity, we only examined the pixel-wise temporal correlation (R) between the other three L-VOD products (i.e., SMOS-IC, MT-DCA and SMAP-IB) and NDVI, as shown in Fig. 10. By exhibiting relatively high R values over Sahel, southern Africa, eastern US, eastern Brazil, Siberian boreal forests and Australia and non-significant ($p > 0.05$) R values over the desert and low inter-annual vegetation dynamic areas (e.g., tropical intact forests), similar spatial distributions of the temporal R values were generally found for the three L-VOD products. In addition, there was asynchrony between the three L-VOD estimates and NDVI over southeast China, Indochina Peninsula and Miombo woodlands, with negative R values below than - 0.5 for the latter area. This decoupling signature originates from the time lags between L-VOD and NDVI due to their different sensitivities to the woody and leafy vegetation components and the decoupling of vegetation water content from foliar greenness, consistent with the findings of Tian et al. (2018) and Li et al. (2021).

The L-VOD product which presented the strongest per-pixel temporal R with NDVI (by considering an absolute difference of R value larger than 0.1) is also provided (Fig. 10d). When discarding non-significant relationships ($p > 0.05$), SMAP-IB L-VOD exhibited the highest R values with NDVI over 33.55% of the pixels, mainly distributed over central Australia, Miombo woodlands, central Europe and Western US, followed by MT-DCA and SMOS-IC, which account for 30.01% and 29.86% of the pixels, respectively. SMOS-IC presented the highest R values over south America, Mexico, central US, Alaska and southeastern Africa. When only considering SMAP-based products (Fig. 10b,c), SMAP-IB was better correlated with NDVI than MT-DCA in particular over middle and low latitudes, e.g., central Australia, Africa and Contiguous US, while MT-DCA performed better over higher latitudes, e.g., over most of the Russian boreal region and Alaska.

To better understand the seasonal dynamics of the different L-VOD products, several pixels with different vegetation types and climates were selected to investigate their time series (Fig. 11). The seasonal dynamics of the five L-VOD products were synchronized with NDVI over most of the non-forest types, except for woody savannas in the Miombo woodlands (Fig. 11b), which is consistent with Fig. 10. Over this latter area, most of the L-VOD products showed a negative correlation with NDVI, except for SCA-V L-VOD, which was estimated from a NDVI

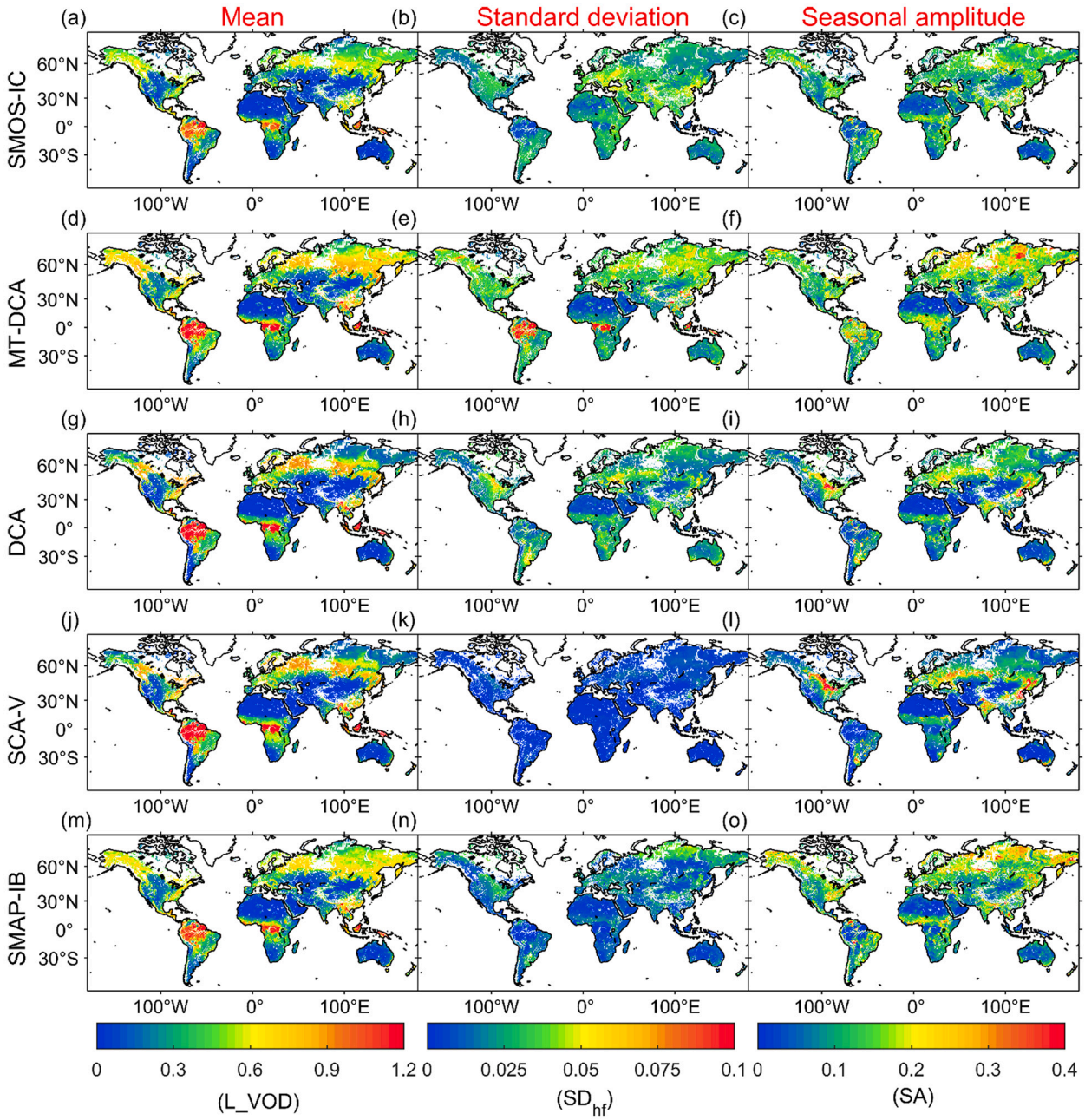

Fig. 8. Global distribution of time averaged, standard deviation of the high-frequency variations (SD_{hf}) and mean annual seasonal amplitude (SA) of the different L-VOD products from April 2015 to March 2019 for a-c) SMOS-IC, d-f) MT-DCA, g-i) DCA, j-l) SCA-V and m-o) SMAP-IB. Note that SD_{hf} was computed after removing the seasonal trend.

climatology. Interestingly, although DCA L-VOD was initialized from a NDVI climatology, it exhibited asynchrony with NDVI at this site. However, over the evergreen broadleaf Amazon forest site with a higher vegetation density (Fig. 11a), DCA L-VOD exhibited very similar characteristics as SCA-V L-VOD, showing almost constant time series similarly to NDVI, whereas the three other L-VOD estimates presented larger temporal variations. At this site, SMAP-IB tended to be smoother, while MT-DCA presented a strong high frequency variability, which explained the higher SD_{hf} values of MT-DCA over tropical forests in Fig. 8e. The open shrublands site (Fig. 11c) in the south of Australia exhibited another exception: while the other four L-VOD products showed distinct dynamics like NDVI, SCA-V L-VOD had small fluctuations. When only considering products independent of NDVI, SMAP-IB, MT-DCA and SMOS-IC were generally found to have similar seasonal dynamics, and they all fluctuated more strongly when L-VOD is relatively low and when rainfall occurs. However, the amplitude of this seasonal dynamics varied depending on the sites. For instance, over the cropland/natural vegetation mosaic site (Fig. 11e), SMAP-IB exhibited a higher seasonal dynamic than MT-DCA and SMOS-IC.

4. Discussion

Based on the evaluation and inter-comparison results shown above in Section 3.2 for SM and Section 3.3 for L-VOD, it was generally found that no algorithm showed an absolute advantage over the others with respect to different error metrics, whether SM and L-VOD were considered together or separately. This is consistent with the previous evaluation results of SM (Al-Yaari et al., 2019; Ma et al., 2019) and VOD retrievals

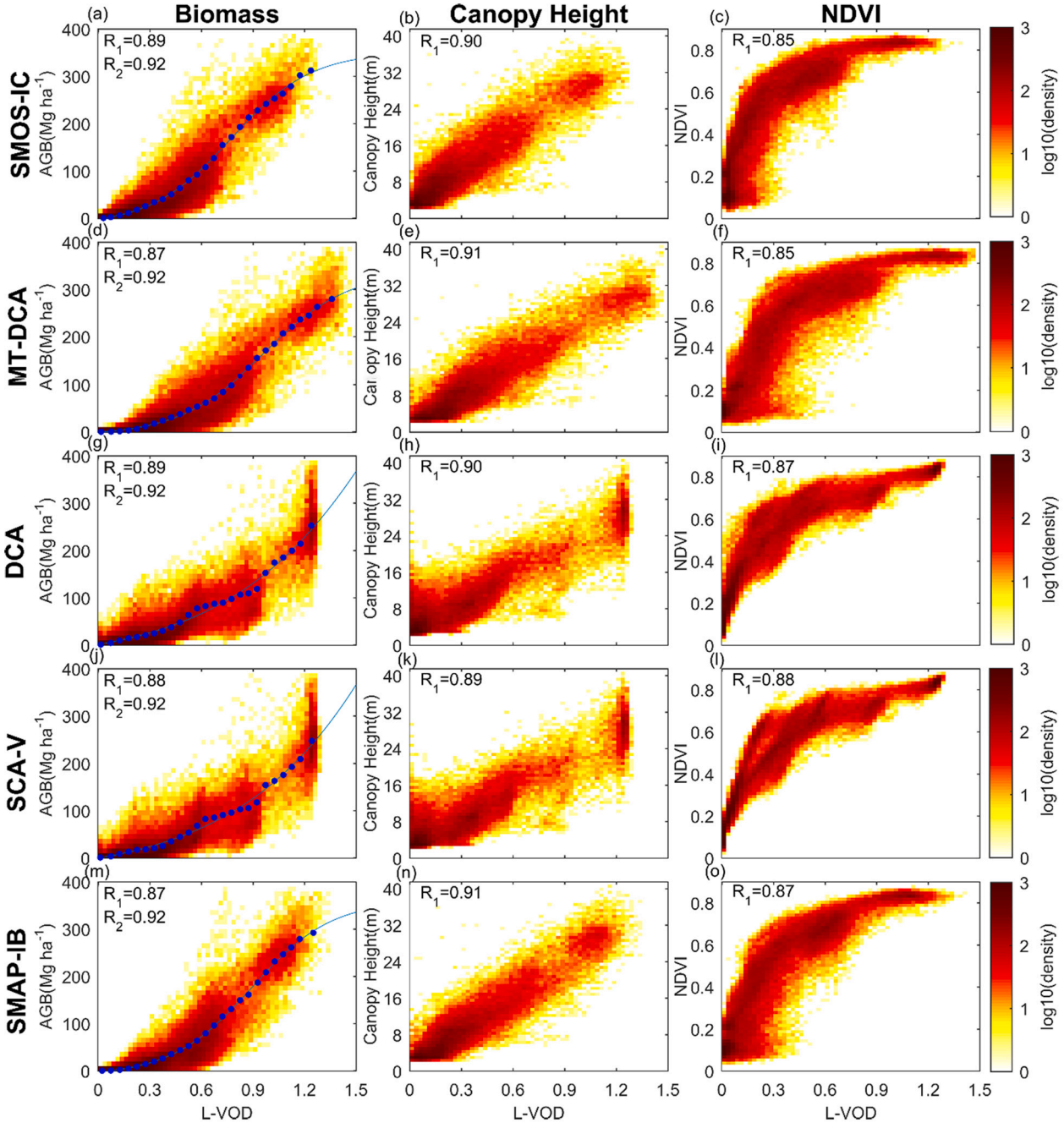

Fig. 9. Density scatter plots of the five L-VOD products (time averaged values) against AGB (first column), canopy height (second column) and NDVI (last column) at the global scale. The blue circles correspond to the distribution of mean AGB values in bins of L-VOD, while the fitting relationships between L-VOD and AGB are displayed as solid blue lines using the function as in Li et al. (2021). R_1 is the spatial correlation coefficient between L-VOD and corresponding proxies, while R_2 is the correlation between predicted AGB (based on L-VOD using above non-linear function) and reference AGB. (For interpretation of the references to colour in this figure legend, the reader is referred to the web version of this article.)

(Li et al., 2021) of these algorithms, although these previous studies did not use exactly the same versions of the products as here. Nevertheless, to simultaneously retrieve SM and L-VOD from the mono-angle SMAP observations while remaining as independent as possible from auxiliary data, we have implemented a multi-temporal (MT) retrieval approach in SMAP-IB leaning on the findings made in SMOS-IC version 2 (Wigneron et al., 2021). Conversely to MT-DCA, the MT approach used in SMAP-IB not only considers the fact that L-VOD changes slowly over time, but also considers that the initial value of SM may change with time and space, rather than using a constant value as in SMOS-IC. This innovative approach led to good performances for both SM and L-VOD as shown in the inter-comparison with other products:

– For SM retrievals, when evaluated against ISMN *in-situ* measurements, SMAP-IB SM exhibited highest overall temporal correlation ($R = 0.74$) followed by MT-DCA ($R = 0.71$), and best scores for R were also obtained by SMAP-IB over most of the networks (15 over 19, Table 3), sites (Fig. 5) or vegetation conditions (Figs. 6 and 7). Conversely, DCA obtained best scores for *ub*RMSD (*ub*RMSD = 0.056 m^3/m^3), followed closely by SCA-V and SMAP-IB (*ub*RMSD ~ 0.058 m^3/m^3). It should be noted that the R values (in particular for SMAP DCA and SCA-V) obtained here are in line with a recent validation

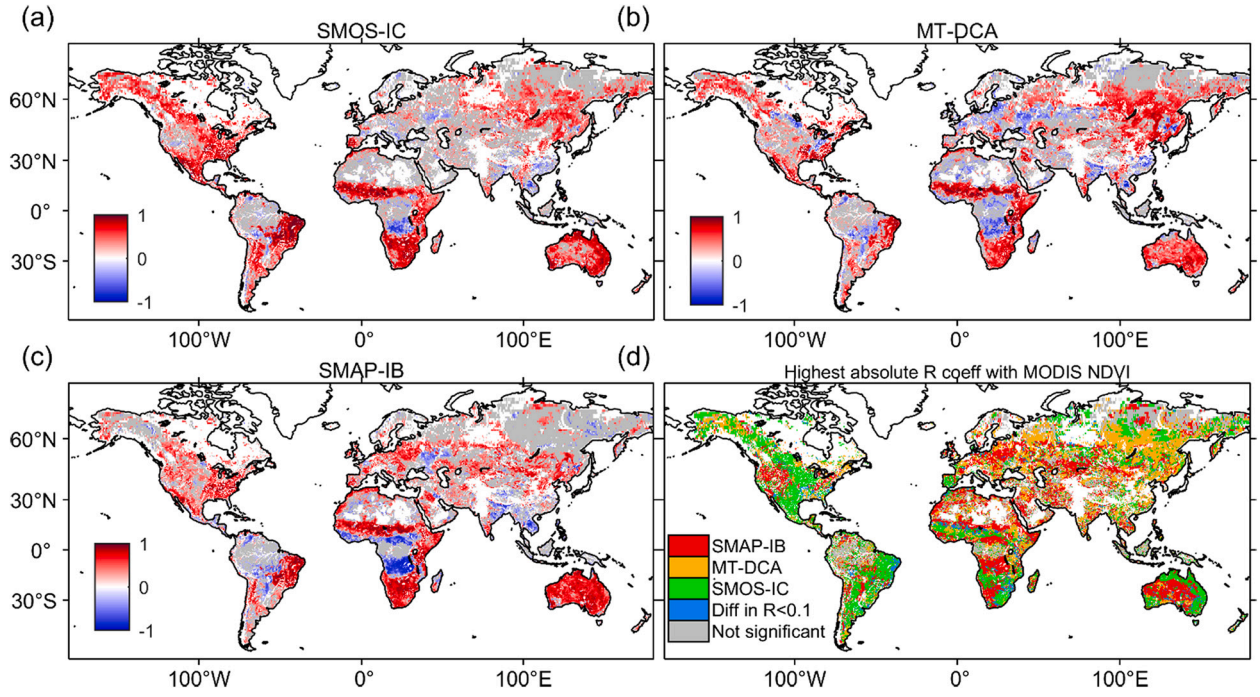

Fig. 10. Pixel-wise temporal correlation (R) between 16-day average values of L-VOD and MODIS NDVI from April 2015 to March 2019 for a) SMOS-IC, b) MT-DCA, c) SMAP-IB, d) maps of above three L-VOD products showing the highest absolute R values with NDVI. Pixels with non-significant ($p > 0.05$) R values are shown in gray. White areas mean "no valid data".

study using sparse network grassland sites, but with a slightly higher *ub*RMSD value (Fig. 4 and Table VIII in Colliander et al., 2021), and also larger than those reported by Chan et al. (2016) and Colliander et al. (2017). The former discrepancy is due to the fact that our study was carried out at the 36 km spatial resolution, while Colliander et al. (2021) evaluated the SMAP 9 km enhanced product. The latter discrepancy may be due to the fact we used more sparse networks from ISMN, which may be affected by representativeness errors (Al-Yaari et al., 2019). Thus, it was not expected that the overall results obtained in this study could achieve very similar values as those reported by Chan et al. (2016) and Colliander et al. (2017) using the core sites. Moreover, we considered more vegetation types (including forests). But interestingly, as in Ayres et al. (2021), we also found a good potential of SMAP for SM retrieval in forest areas.

– For VOD retrievals, as there is a lack of reference values from *in-situ* observations or models to do a direct inter-comparison, we only implemented an indirect evaluation based on vegetation-related proxies at the global scale by using semi-monthly L-VOD observations as done in (Li et al., 2021; Wigneron et al., 2021). An assessment for specific terrestrial ecosystems (e.g., Africa, tropical and boreal forests) or different seasons may provide a more detailed understanding of the performances of the different L-VOD products (Rodríguez-Fernández et al., 2018; Fan et al., 2019; Mialon et al., 2020). Noting these limitations, we found that, consistently, better scores were generally obtained for SMAP-IB, MT-DCA and SMOS-IC for all the criteria: relatively high temporal (Fig. 10) or spatial (Table S8) correlation (R) values between NDVI and L-VOD were found especially over short vegetation types and all three products presented a smooth non-linear relationship with AGB and a good linear relationship with tree height, even for tall forests (Fig. 9). However, this was not the case for the L-VOD products (i.e., DCA and SCA-V) incorporating NDVI information, which exhibited a certain degree of saturation. Nevertheless, it was interesting to find that DCA L-VOD also exhibited asynchrony with NDVI over the Miombo woodlands (Figs. 11b and S3), like the other L-VOD products which were independent of the optical vegetation index. This may be related to the value of the regularization parameter (λ) in DCA, which was used to determine the degree of freedom to converge to values far enough from the initial value (Chaubell et al., 2020; O'Neill et al., 2020). This signature also reminded us that the differences in the L-VOD spatial patterns shown in Fig. 8 (especially in the high latitudes) between DCA and the other products may also be due to the different H_R and ω values used by each product as summarized in Table 2 of Li et al. (2021) and Chaubell et al. (2020).

Although SMAP-IB presented good performances for both SM and L-VOD, there is still room to improve this first version (V1) of the algorithm in the next step. For instance, SMAP-IB had a relatively poor performance in SM retrievals over woody savannas (Fig. 7) when evaluated against the ISMN observations and a strange high seasonal L-VOD amplitude in the very high latitudes (above ~60°N) (Fig. 8). The former result relative to the SM retrievals may lead us to consider performing an update of the calibration parameters including both H_R and ω (Table S1) over woody savannas, as the current values were derived from the calibration of Fernandez-Moran et al. (2017a) based on a different retrieval approach. The latter case relative to the L-VOD retrievals may lead us to consider to improve the algorithms considering the specific environmental conditions of the boreal regions. For instance, the frozen conditions may interrupt the MT method used in this study (Wigneron et al., 2021), and the presence of a large amount of soil organic matter (SOM) may require the use of a specific soil dielectric model (Mironov et al., 2019). Another possible reason explaining the SMAP-IB results in the boreal regions could be related to the distortion of EASE-Grid V2.0 at high latitudes when using global cylindrical projection (Colliander et al., 2021). In addition, uncertainties associated with the pixel heterogeneity may also affect the L-VOD retrievals and need to be considered in the inversion, as a certain degree of distortion was found in the density distribution between the multiple L-VOD products and AGB (Fig. 9 a, d & m).

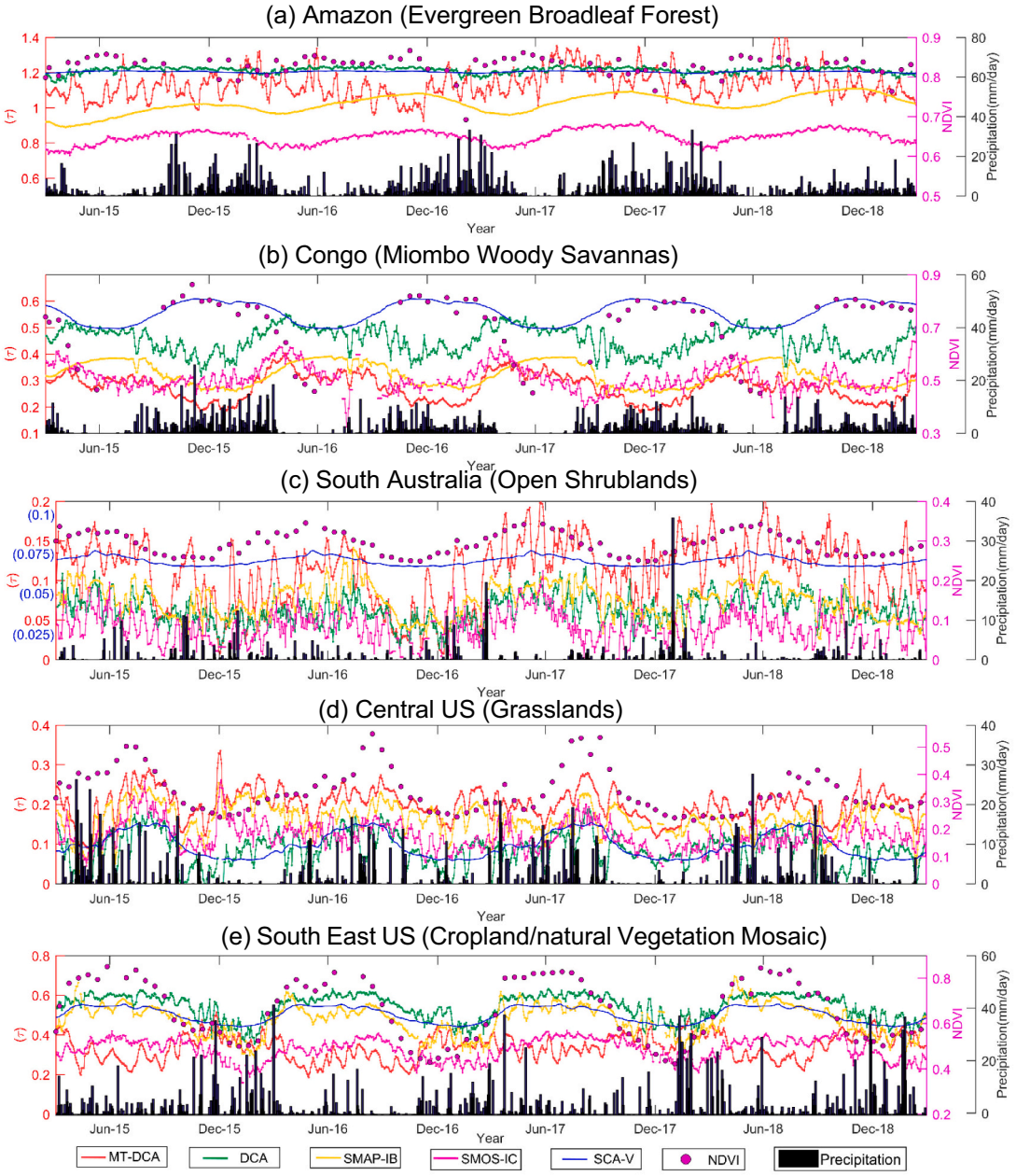

Fig. 11. Temporal series of the five L-VOD products (smoothed with a 7-day moving window filter) over selected pixels between April 2015 and March 2019. Each plot also contains daily precipitation (mm/day) and NDVI information. Note: the scale value of SCA-V in Fig. 11c is marked in blue, and the latitude and longitude information of these pixels are shown in Table S9. (For interpretation of the references to colour in this figure legend, the reader is referred to the web version of this article.)

5. Concluding remarks and outlook

This paper presents a new mono-angle retrieval algorithm (referred to SMAP-IB) for SM and L-VOD from the dual-channel SMAP L-band radiometric observations. The main features of SMAP-IB were illustrated by assessing and inter-comparing it with four other satellite SM and L-VOD products (i.e., MT-DCA, SMAP new version DCA, SCA-V and SMOS-IC) during April 2015–March 2019. To achieve this, the skills of all five SM products in capturing the temporal variations of *in-situ* observations from ISMN were evaluated, while the L-VOD products were evaluated against vegetation-related proxies including AGB, tree height and NDVI from a spatial and temporal perspective.

We found that SMAP-IB performs well for both SM and L-VOD. In terms of SM retrievals, SMAP-IB obtained best scores for capturing the temporal variations of ISMN SM, with an overall median R value of 0.74. Regarding *ub*RMSD, while the lowest value was obtained by SMAP new version DCA (*ub*RMSD = 0.056 m^3/m^3), SMAP-IB and SCA-V had both very close scores (*ub*RMSD ~ 0.058 m^3/m^3). Considering different vegetation conditions, SMAP-IB showed best scores for correlation and similar scores to SCA-V for *ub*RMSD over most of the vegetation types except for woody savannas. Overall, SMAP-IB SM retrievals presented best scores for R, *ub*RMSD and Bias (0.002 m^3/m^3) among the three products independent of NDVI (the other two are MT-DCA and SMOS-IC). With respect to L-VOD, SMAP-IB had good performances in both space and time. In particular, similar to SMOS-IC and MT-DCA, SMAP-IB L-VOD correlated well with aboveground biomass and tree height, with spatial R values of ~0.88 and ~ 0.90, respectively. All three L-VOD retrievals presented a smooth non-linear density distribution with AGB

and a good linear relationship with tree height, even for tall forests. While exhibiting a higher seasonal amplitude in the high latitudes (above ~60°N), SMAP-IB was generally found to show similar seasonal vegetation dynamics to those of MT-DCA and SMOS-IC, and all of them could well capture the short-vegetation dynamics expressed by NDVI.

Other conclusions, non-specific to SMAP-IB, could also be drawn from the results: i) the SMAP new version DCA SM retrievals had similar (or slightly better) performance to SCA-V with respect to both correlations and *ub*RMSD, while they both exhibited acceptable accuracy over some forest types (comparable to non-forest types), although forest types were typically triggered as non-recommended values; ii) considering different L-VOD ranges parameterizing the vegetation effects, we found the temporal R values of all five SM products presented a relatively low sensitivity to vegetation effects, while the *ub*RMSD metric was relatively more sensitive to these effects; iii) notable differences between MT-DCA L-VOD and the four other products were found over tropical forests concerning absolute values, standard deviations and seasonal amplitudes; iv) the new version of DCA initialized with NDVI climatology may integrate optical information from the latter as its density distribution had a similar dispersion and distribution shape to SCA-V, and both showed obvious saturation effects at L-VOD ~ 1.2, and AGB around ~250 Mg ha^{-1} or tree height around ~28 m.

Our results suggest that cautions may need to be taken when using *a priori* information to constrain retrievals in microwave models, because of the likelihood that the final retrievals are dependent on it. This lack of independence (as found here for DCA) may limit the interest of using DCA L-VOD for monitoring the vegetation dynamics (phenology, carbon cycle, etc.). Moreover, it may reduce the possibility of developing complementary applications between microwave data sources (usually coarse resolution) and high-resolution optical-near infrared remote sensing data (Li et al., 2021). Considering that SMAP-IB exhibits a good compromise in terms of high accuracy for both SM and L-VOD, in a future step, we will apply it to the SMOS observation at the angle of 40° to promote the fusion of the SMOS and SMAP products. This step is important to ensure the continuity of L-band SM and L-VOD observations, in view of the possible failing of one of the sensors (SMOS or SMAP) in the near future. Note that the retrieval approach of the SMAP-IB algorithm proposed here to solve the ill-posed issue of simultaneously retrieving SM and VOD from one-angle and dual-polarization observations can also be extended to other passive microwave satellites (e.g., AMSR2).

Data availability

SMAP-IB was developed by INRAE (Institut national de recherche pour l'agriculture, l'alimentation et l'environnement) Bordeaux and will be made available at the INRAE Bordeaux remote sensing lab website (https://ib.remote-sensing.inrae.fr/).

Declaration of Competing Interest

The authors declare that they have no conflict of interest.

Acknowledgments

This study was jointly funded by CNES, France (Centre National d'Etudes Spatiales), the China Scholarship Council (201804910838) and the National Natural Science Foundation of China (Grant No.42171339). A partial contribution to this work was made at Jet Propulsion Laboratory, California Institute of Technology under a contract with the National Aeronautics and Space Administration. Ardeshir Ebtehaj's effort was supported by an award from the NASA's Remote Sensing Theory Program (80NSSC20K1717).

Appendix A. Supplementary data

Supplementary data to this article can be found online at https://doi.org/10.1016/j.rse.2022.112921.

References

Abowarda, A.S., Bai, L., Zhang, C., Long, D., Li, X., Huang, Q., Sun, Z., 2021. Generating surface soil moisture at 30 m spatial resolution using both data fusion and machine learning toward better water resources management at the field scale. Remote Sens. Environ. 255, 112301. https://doi.org/10.1016/j.rse.2021.112301.

Al Bitar, A., Mialon, A., Kerr, Y.H., Cabot, F., Richaume, P., Jacquette, E., Quesney, A., Mahmoodi, A., Tarot, S., Parrens, M., 2017. The global SMOS level 3 daily soil moisture and brightness temperature maps. Earth Syst. Sci. Data 9, 293–315.

Albergel, C., Rüdiger, C., Pellarin, T., Calvet, J.-C., Fritz, N., Froissard, F., Suquia, D., Petitpa, A., Piguet, B., Martin, E., 2008. From near-surface to root-zone soil moisture using an exponential filter: an assessment of the method based on in-situ observations and model simulations. Hydrol. Earth Syst. Sci. 12, 1323–1337.

Al-Yaari, A., Wigneron, J.P., Ducharne, A., Kerr, Y., de Rosnay, P., de Jeu, R., Govind, A., Al Bitar, A., Albergel, C., Muñoz-Sabater, J., Richaume, P., Mialon, A., 2014. Global-scale evaluation of two satellite-based passive microwave soil moisture datasets (SMOS and AMSR-E) with respect to land data assimilation system estimates. Remote Sens. Environ. 149, 181–195.

Al-Yaari, A., Dayau, S., Chipeaux, C., Aluome, C., Kruszewski, A., Loustau, D., Wigneron, J.-P., 2018. The AQUI soil moisture network for satellite microwave remote sensing validation in South-Western France. Remote Sens. 10, 1839.

Al-Yaari, A., Wigneron, J.P., Dorigo, W., Colliander, A., Pellarin, T., Hahn, S., Mialon, A., Richaume, P., Fernandez-Moran, R., Fan, L., Kerr, Y.H., De Lannoy, G., 2019. Assessment and inter-comparison of recently developed/reprocessed microwave satellite soil moisture products using ISMN ground-based measurements. Remote Sens. Environ. 224, 289–303.

Al-Yaari, A., Wigneron, J.-P., Philippe, P., Reichstein, M., Ballantyne, A., Ogée, J., Ducharne, A., Swenson, J.J., Frappart, F., Fan, L., Wingate, L., Li, X., Hufkens, K., Knapp, A.K., 2020. Asymmetric responses of ecosystem productivity to rainfall anomalies vary inversely with mean annual rainfall over the conterminous U.S. Glob. Chang. Biol. 00, 1–15.

Anderson, M.C., Norman, J.M., Kustas, W.P., Houborg, R., Starks, P.J., Agam, N., 2008. A thermal-based remote sensing technique for routine mapping of land-surface carbon, water and energy fluxes from field to regional scales. Remote Sens. Environ. 112 (12), 4227–4241.

Ayres, E., Colliander, A., Cosh, M., Roberti, A., J., Simkin, S., & Genazzio, M.A.., 2021. Validation of SMAP Soil Moisture at Terrestrial National Ecological Observatory Network (NEON) Sites Show Potential for Soil Moisture Retrieval in Forested Areas. TechRxiv. Preprint. https://doi.org/10.36227/techrxiv.14681298.v1.

Bai, L., Lv, X., Li, X., 2019. Evaluation of two SMAP soil moisture retrievals using modeled-and ground-based measurements. Remote Sens. 11 (24), 2891.

Bell, J.E., Palecki, M.A., Baker, C.B., Collins, W.G., Lawrimore, J.H., Leeper, R.D., Hall, M.E., Kochendorfer, J., Meyers, T.P., Wilson, T., 2013. US climate reference network soil moisture and temperature observations. J. Hydrometeorol. 14, 977–988.

Blöschl, G., Blaschke, A.P., Broer, M., Bucher, C., Carr, G., Chen, X., Eder, A., Exner-Kittridge, M., Farnleitner, A., Flores-Orozco, A., Haas, P., Hogan, P., Kazemi Amiri, A., Oismüller, M., Parajka, J., Silasari, R., Stadler, P., Strauss, P., Vreugdenhil, M., Wagner, W., Zessner, M., 2016. The hydrological open air laboratory (HOAL) in Petzenkirchen: a hypothesis-driven observatory. Hydrol. Earth Syst. Sci. 20, 227–255.

Brandt, M., Wigneron, J.P., Chave, J., Tagesson, T., Penuelas, J., Ciais, P., Rasmussen, K., Tian, F., Mbow, C., Al-Yaari, A., Rodriguez-Fernandez, N., Schurgers, G., Zhang, W., Chang, J., Kerr, Y., Verger, A., Tucker, C., Mialon, A., Rasmussen, L.V., Fan, L., Fensholt, R., 2018. Satellite passive microwaves reveal recent climate-induced carbon losses in African drylands. Nat. Ecol. Evol. 2, 827–835.

Brodzik, M.J., Knowles, K., 2011. EASE-Grid 2.0 Land Cover Classifications Derived from Boston University MODIS/Terra Land Cover Data, Version 1. NASA National Snow and Ice Data Center Distributed Active Archive Center, Boulder, Colorado USA. https://doi.org/10.5067/XR8523MC24TB.

Chan, S.K., Bindlish, R., Hunt, R., Jackson, T.J., Kimball, J.S., 2013. SMAP Ancillary Data Report Vegetation Water Content; Version 1. Jet Propulsion Laboratory, Pasadena, CA, USA.

Chan, S., Bindlish, Rajat, O'Neill, Peggy, Njoku, Eni, Jackson, Tom, Colliander, Andreas, Chen, Fan, Burgin, Mariko, Dunbar, Scott, Piepmeier, Jeffrey, Yueh, Simon, Entekhabi, Dara, Cosh, Michael H., Caldwell, Todd, Walker, Jeffrey, Wu, Xiaoling, Berg, Aaron, Rowlandson, Tracy, Pacheco, Anna, McNairn, Heather, Thibeault, Marc, Martínez-Fernández, José, González-Zamora, Ángel, Seyfried, Mark, Bosch, David, Starks, Patrick, Goodrich, David, Prueger, John, Palecki, Michael, Small, Eric E., Zreda, Marek, Calvet, Jean-Christophe, Crow, Wade T., Kerr, Y., 2016. Assessment of the SMAP passive soil moisture product. IEEE Trans. Geosci. Remote Sens. 54, 4994–5007.

Chaubell, M.J., Yueh, S.H., Dunbar, R.S., Colliander, A., Dunbar, R.S., Chen, F., Chan, S. K., Entekhabi, D., Bindlish, R., O'Neill, P., et al., 2020. Improved SMAP Dual-Channel algorithm for the retrieval of soil moisture. IEEE Trans. Geosci. Remote Sens. 58 (6), 3894–3905.

Colliander, A., Jackson, T.J., Bindlish, R., Chan, S., Das, N.N., Kim, S., Cosh, M.H., Dunbar, R.S., Dang, L., Pashaian, L., 2017. Validation of SMAP surface soil moisture products with core validation sites. Remote Sens. Environ. 191, 215–231.

Colliander, A., Reichle, R., Crow, W., Cosh, M., Chen, F., Chan, S., Yueh, S., 2021. Validation of Soil Moisture Data Products from the NASA SMAP Mission.
Crow, W.T., Chan, S.K., Entekhabi, D., Houser, P.R., Hsu, A.Y., Jackson, T.J., Njoku, E.G., O'Neill, P.E., Shi, J., Zhan, X., 2005. An observing system simulation experiment for hydros radiometer-only soil moisture products. IEEE Trans. Geosci. Remote Sens. 43 (6), 1289–1303.
Dobriyal, P., Qureshi, A., Badola, R., Hussain, S.A., 2012. A review of the methods available for estimating soil moisture and its implications forwater resource management. J. Hydrol. 458–459, 110–117.
Dong, J., Crow, W.T., Bindlish, R., 2018. The error structure of the SMAP single and dual channel soil moisture retrievals. Geophys. Res. Lett. 45, 758–765.
Dorigo, W., Xaver, A., Vreugdenhil, M., Gruber, A., Hegyiova, A., Sanchis-Dufau, A., Zamojski, D., Cordes, C., Wagner, W., Drusch, M., 2013. Global automated quality control of in situ soil moisture data from the international soil moisture network. Vadose Zone J. 12.
Dorigo, W., Himmelbauer, I., Aberer, D., Schremmer, L., Petrakovic, I., Zappa, L., Sabia, R., 2021. The international soil moisture network: serving earth system science for over a decade. Hydrol. Earth Syst. Sci. Discuss. 1–83.
Ebtehaj, A., Bras, R.L., 2019. A physically constrained inversion for super-resolved passive microwave retrieval of soil moisture and vegetation water content in L-band. Remote Sens. Environ. 233, 111346.
Entekhabi, D., Njoku, E.G., O'Neill, P.E., Kellogg, K.H., Crow, W.T., Edelstein, W.N., Entin, J.K., Goodman, S.D., Jackson, T.J., Johnson, J., 2010a. The soil moisture active passive (SMAP) mission. Proc. IEEE 98, 704–716.
Entekhabi, D., Reichle, R.H., Koster, R.D., Crow, W.T., 2010b. Performance metrics for soil moisture retrievals and application requirements. J. Hydrol. 11, 832–840.
Fan, L., Wigneron, J.P., Ciais, P., Chave, J., Brandt, M., Fensholt, R., Saatchi, S.S., Bastos, A., Al-Yaari, A., Hufkens, K., Qin, Y., Xiao, X., Chen, C., Myneni, R.B., Fernandez-Moran, R., Mialon, A., Rodriguez-Fernandez, N.J., Kerr, Y., Tian, F., Penuelas, J., 2019. Satellite-observed pantropical carbon dynamics. Nat. Plant 5, 944–951.
Feldman, A.F., Short Gianotti, D.J., Konings, A.G., McColl, K.A., Akbar, R., Salvucci, G. D., Entekhabi, D., 2018. Moisture pulse-reserve in the soil-plant continuum observed across biomes. Nat. Plant 4, 1026–1033.
Fernandez-Moran, R., Wigneron, J.P., De Lannoy, G., Lopez-Baeza, E., Parrens, M., Mialon, A., Mahmoodi, A., Al-Yaari, A., Bircher, S., Al Bitar, A., Richaume, P., Kerr, Y., 2017a. A new calibration of the effective scattering albedo and soil roughness parameters in the SMOS SM retrieval algorithm. Int. J. Appl. Earth Obs. Geoinf. 62, 27–38.
Fernandez-Moran, R., Al-Yaari, A., Mialon, A., Mahmoodi, A., Al Bitar, A., De Lannoy, G., Rodriguez-Fernandez, N., Lopez-Baeza, E., Kerr, Y., Wigneron, J.-P., 2017b. SMOS-IC: an alternative SMOS soil moisture and vegetation optical depth product. Remote Sens. 9.
Frappart, F., Wigneron, J.-P., Li, X., Liu, X., Al-Yaari, A., Fan, L., Wang, M., Moisy, C., Le Masson, E., Aoulad Lafkih, Z., Vallé, C., Ygorra, B., Baghdadi, N., 2020. Global monitoring of the vegetation dynamics from the vegetation optical depth (VOD): a review. Remote Sens. 12, 2915.
Gao, L., Sadeghi, M., Ebtehaj, A., 2020a. Microwave retrievals of soil moisture and vegetation optical depth with improved resolution using a combined constrained inversion algorithm: application for SMAP satellite. Remote Sens. Environ. 239, 111662.
Gao, L., Sadeghi, M., Feldman, A.F., Ebtehaj, A., 2020b. A spatially constrained multichannel algorithm for inversion of a first-order microwave emission model at L-band. IEEE Trans. Geosci. Remote Sens. 58 (11), 8134–8146.
Gao, L., Sadeghi, M., Ebtehaj, A., Wigneron, J.-P., 2020c. A temporal polarization ratio algorithm for calibration-free retrieval of soil moisture at L-band. Remote Sens. Environ. 249, 112019.
Gao, L., Ebtehaj, A., Chaubell, M.J., Sadeghi, M., Li, X., Wigneron, J.-P., 2021. Reappraisal of SMAP inversion algorithms for soil moisture and vegetation optical depth. Remote Sens. Environ. 264.
González-Zamora, Á., Sánchez, N., Pablos, M., Martínez-Fernández, J., 2019. CCI soil moisture assessment with SMOS soil moisture and in situ data under different environmental conditions and spatial scales in Spain. Remote Sens. Environ. 225, 469–482.
Grant, J.P., Wigneron, J.P., De Jeu, R.A.M., Lawrence, H., Mialon, A., Richaume, P., Al Bitar, A., Drusch, M., van Marle, M.J.E., Kerr, Y., 2016. Comparison of SMOS and AMSR-E vegetation optical depth to four MODIS-based vegetation indices. Remote Sens. Environ. 172, 87–100.
Gruber, Alexander, Lannoy, De, Gabrielle, Albergel, Cl'ement, Al-Yaari, Amen, Luca, Brocca, Calvet, Colliander, Andreas, Cosh, Michael, Crow, Wade, Dorigo, Wouter, 2020. Validation practices for satellite soil moisture retrievals: what are (the) errors ? Remote Sens. Environ. 244, 111806.
Hersbach, H., Bell, B., Berrisford, P., Hirahara, S., Horányi, A., Muñoz-Sabater, J., Thépaut, J.N., 2020. The ERA5 global reanalysis. Q. J. R. Meteorol. Soc. 146 (730), 1999–2049.
Hmimina, G., Dufrêne, E., Pontailler, J.Y., Delpierre, N., Aubinet, M., Caquet, B., Soudani, K., 2013. Evaluation of the potential of MODIS satellite data to predict vegetation phenology in different biomes: an investigation using ground-based NDVI measurements. Remote Sens. Environ. 132, 145–158.
Hovmöller, E., 1949. The trough-and-ridge diagram. Tellus 1, 62–66.
Huffman, G.J., Stocker, E.F., Bolvin, D.T., Nelkin, E.J., Jackson, T., 2019. GPM IMERG Late Precipitation L3 1 Day 0.1 Degree x 0.1 Degree V06. NASA's Precipitation Processing Center, Greenbelt, Maryland. https://doi.org/10.5067/GPM/IMERGDL/DAY/06.
Jackson, T.J., 1993. III. Measuring surface soil moisture using passive microwave remote sensing. Hydrol. Process. 7, 139–152.
Jackson, T.J., Le Vine, D.M., Hsu, A.Y., Oldak, A., Starks, P.J., Swift, C.T., Isham, J.D., Haken, M., 1999. Soil moisture mapping at regional scales using microwave radiometry: the Southern Great Plains hydrology experiment. IEEE Trans. Geosci. Remote Sens. 37 (5), 2136–2151.
Jackson, T.J., Cosh, M.H., Bindlish, R., Starks, P.J., Bosch, D.D., Seyfried, M., Goodrich, D.C., Moran, M.S., Du, J., 2010. Validation of advanced microwave scanning radiometer soil moisture products. IEEE Trans. Geosci. Remote Sens. 48, 4256–4272.
Jung, M., Reichstein, M., Schwalm, C.R., Huntingford, C., Sitch, S., Ahlström, A., Arneth, A., Camps-Valls, G., Ciais, P., Friedlingstein, P., 2017. Compensatory water effects link yearly global land CO 2 sink changes to temperature. Nature 541, 516.
Kang, C.S., Kanniah, K.D., Kerr, Y.H., 2019. Calibration of SMOS soil moisture retrieval algorithm: a case of tropical site in Malaysia. IEEE Trans. Geosci. Remote Sens. 57 (6), 3827–3839.
Karthikeyan, L., Pan, M., Konings, A.G., Piles, M., Fernandez-Moran, R., Nagesh Kumar, D., Wood, E.F., 2019. Simultaneous retrieval of global scale vegetation optical depth, surface roughness, and soil moisture using X-band AMSR-E observations. Remote Sens. Environ. 234, 111473.
Kerr, Y.H., Waldteufel, P., Wigneron, J.-P., Delwart, S., Cabot, F., Boutin, J., Escorihuela, M.-J., Font, J., Reul, N., Gruhier, C., 2010. The SMOS mission: new tool for monitoring key elements ofthe global water cycle. Proc. IEEE 98, 666–687.
Kerr, Y.H., Waldteufel, P., Richaume, P., Wigneron, J.P., Ferrazzoli, P., Mahmoodi, A., Al Bitar, A., Cabot, F., Gruhier, C., Juglea, S.E., Leroux, D., Mialon, A., Delwart, S., 2012. The SMOS soil moisture retrieval algorithm. Geosci. Remote Sens. IEEE Trans. 50, 1384–1403.
Kerr, Y.H., Al-Yaari, A., Rodriguez-Fernandez, N., Parrens, M., Molero, B., Leroux, D., Bircher, S., Mahmoodi, A., Mialon, A., Richaume, P., Delwart, S., Al Bitar, A., Pellarin, T., Bindlish, R., Jackson, T.J., Rudiger, C., Waldteufel, P., Mecklenburg, S., Wigneron, J.-P., 2016. Overview ofSMOS performance in terms of global soil moisture monitoring after six years in operation. Remote Sens. Environ. 180, 40–63.
Konings, A.G., Piles, M., Rötzer, K., McColl, K.A., Chan, S.K., Entekhabi, D., 2016. Vegetation optical depth and scattering albedo retrieval using time series of dual-polarized L-band radiometer observations. Remote Sens. Environ. 172, 178–189.
Konings, A.G., Piles, M., Das, N., Entekhabi, D., 2017. L-band vegetation optical depth and effective scattering albedo estimation from SMAP. Remote Sens. Environ. 198, 460–470.
Koster, R.D., Dirmeyer, P.A., Guo, Z., Bonan, G., Chan, E., Cox, P., Gordon, C., Kanae, S., Kowalczyk, E., Lawrence, D., 2004. Regions of strong coupling between soil moisture and precipitation. Science 305, 1138–1140.
Kurum, M., 2013. Quantifying scattering albedo in microwave emission of vegetated terrain. Remote Sens. Environ. 129, 66–74.
Lang, N., Kalischek, N., Armston, J., Schindler, K., Dubayah, R., Wegner, J.D., 2021. Global canopy height estimation with GEDI LIDAR waveforms and Bayesian deep learning. arXiv Preprint arXiv:2103.03975.
Lebel, T., Cappelaere, B., Galle, S., Hanan, N., Kergoat, L., Levis, S., Vieux, B., Descroix, L., Gosset, M., Mougin, E., 2009. AMMA-CATCH studies in the Sahelian region of WestAfrica: an overview. J. Hydrol. 375, 3–13.
Li, M., Wu, P., Ma, Z., 2020a. A comprehensive evaluation of soil moisture and soil temperature from third-generation atmospheric and land reanalysis data sets. Int. J. Climatol. 1–23.
Li, X., Al-Yaari, A., Schwank, M., Fan, L., Frappart, F., Swenson, J., Wigneron, J.P., 2020b. Compared performances of SMOS-IC soil moisture and vegetation optical depth retrievals based on Tau-Omega and Two-Stream microwave emission models. Remote Sens. Environ. 236, 111502.
Li, X., Wigneron, J.P., Frappart, F., Fan, L., Wang, M., Liu, X., Al-Yaari, A., Moisy, M., 2020c. Development and validation of the SMOS-IC version 2 (V2) soil moisture product. In: IGARSS 2020–2020 IEEE International Geoscience and Remote Sensing Symposium. IEEE.
Li, X., Wigneron, J.P., Frappart, F., Fan, L., Ciais, P., Fensholt, R., Moisy, C., 2021. Global-scale assessment and inter-comparison of recently developed/reprocessed microwave satellite vegetation optical depth products. Remote Sens. Environ. 253, 112208.
Liu, Y.Y., de Jeu, R.A.M., McCabe, M.F., Evans, J.P., van Dijk, A.I.J.M., 2011. Global long-term passive microwave satellite-based retrievals of vegetation optical depth. Geophys. Res. Lett. 38.
Liu, Y.Y., van Dijk, A.I.J.M., de Jeu, R.A.M., Canadell, J.G., McCabe, M.F., Evans, J.P., Wang, G., 2015. Recent reversal in loss of global terrestrial biomass. Nat. Clim. Chang. 5, 470–474.
Liu, A., Cheng, X., Chen, Z., 2021a. Performance evaluation of GEDI and ICESat-2 laser altimeter data for terrain and canopy height retrievals. Remote Sens. Environ. 264, 112571.
Liu, X., Wigneron, J.P., Fan, L., Frappart, F., Ciais, P., Baghdadi, N., Moisy, C., 2021b. ASCAT IB: a radar-based vegetation optical depth retrieved from the ASCAT scatterometer satellite. Remote Sens. Environ. 264, 112587.
Long, D., Yan, L., Bai, L., Zhang, C., Li, X., Lei, H., Yang, H., Tian, F., Zeng, C., Meng, X., Shi, C., 2020. Generation of MODIS-like land surface temperatures under all-weather conditions based on a data fusion approach. Remote Sens. Environ. 246, 111863. https://doi.org/10.1016/j.rse.2020.111863.
Ma, H., Zeng, J., Chen, N., Zhang, X., Cosh, M.H., Wang, W., 2019. Satellite surface soil moisture from SMAP, SMOS, AMSR2 and ESA CCI: A comprehensive assessment using global ground-based observations. Remote Sens. Environ. 231, 111215.
Ma, H., Zeng, J., Zhang, X., Fu, P., Zheng, D., Wigneron, J.-P., Chen, N., Niyogi, D., 2021. Evaluation of six satellite- and model-*based* surface soil temperature datasets using global ground-based observations. Remote Sens. Environ. 264, 112605.

Mialon, A., Rodríguez-Fernández, N.J., Santoro, M., Saatchi, S., Mermoz, S., Bousquet, E., Kerr, Y.H., 2020. Evaluation of the sensitivity of SMOS L-VOD to forest above-ground biomass at global scale. Remote Sens. 12.

Mironov, V.L., Kosolapova, L.G., Fomin, S.V., Savin, I.V., 2019. Experimental analysis and empirical model of the complex permittivity of five organic soils at 1.4 GHz in the temperature range from −30 °C to 25 °C. IEEE Trans. Geosci. Remote Sens. 57, 3778–3787.

Mo, T., Choudhury, B., Schmugge, T., Wang, J., Jackson, T., 1982. A model for microwave emission from vegetation-covered fields. J. Geophys. Res. Ocean 87, 11229–11237.

Moghaddam, M., Entekhabi, D., Goykhman, Y., Li, K., Liu, M., Mahajan, A., Teneketzis, D., 2010. A wireless soil moisture smart sensor web using physics-based optimal control: concept and initial demonstrations. IEEE J. Select. Top. Appl. Earth Observ. Remote Sens. 3 (4), 522–535.

Njoku, E.G., Entekhabi, D., 1996. Passive microwave remote sensing of soil moisture. J. Hydrol. 184 (1–2), 101–129.

Njoku, E.G., Jackson, T.J., Lakshmi, V., Chan, T.K., Nghiem, S.V., 2003. Soil moisture retrieval from AMSR-E. IEEE Trans. Geosci. Remote Sens. 41 (2), 215–229.

O'Neill, P.E., Chan, S., Njoku, E.G., Jackson, T., Bindlish, R., Chaubell, J., 2021. SMAP L3 Radiometer Global Daily 36 km EASE-Grid Soil Moisture, Version 8. NASA National Snow and Ice Data Center Distributed Active Archive Center, Boulder, Colorado USA. https://doi.org/10.5067/OMHVSRGFX38O.

O'Neill, P., Njoku, E., Jackson, T., Chan, S., Bindlish, R., 2015. SMAP Algorithm Theoretical Basis Document: Level 2 & 3 Soil Moisture (Passive) Data Products. Jet Propulsion Lab., California Inst. Technol, Pasadena, CA, USA. JPL D-66480.

O'Neill, P.E., Chan, S., Njoku, E.G., Jackson, T., Bindlish, R., Chaubell, J., 2020. SMAP L3 Radiometer Global Daily 36 km EASE-Grid Soil Moisture, Version 7. NASA National Snow and Ice Data Center Distributed Active Archive Center, Boulder, Colorado USA. https://doi.org/10.5067/HH4SZ2PXSP6A.

Parrens, M., Wigneron, J.-P., Richaume, P., Mialon, A., Bitar, Al, Fernandez-Moran, A., AlYaari, R., Kerr, A., 2016. Global-scale surface roughness effects at L-band as estimated from SMOS observations. Remote Sens. Environ. 181, 122–136.

Peng, J., Mohammed, P., Chaubell, J., Chan, S., Kim, S., Das, N., Dunbar, S., Bindlish, R., Xu, X., 2019. Soil Moisture Active Passive (SMAP) L1-L3 Ancillary Static Data, Version 1. NASA National Snow and Ice Data Center Distributed Active Archive Center, Boulder, Colorado USA. https://doi.org/10.5067/HB8BPJ13TDQJ.

Qin, Y., Xiao, X., Wigneron, J.P., Ciais, P., Brandt, M., Fan, L., Moore, B., 2021. Carbon loss from forest degradation exceeds that from deforestation in the Brazilian Amazon. Nat. Clim. Chang. 1–7.

Rodríguez-Fernández, N.J., Mialon, A., Mermoz, S., Bouvet, A., Richaume, P., Al Bitar, A., Al-Yaari, A., Brandt, M., Kaminski, T., Le Toan, T., Kerr, Y.H., Wigneron, J.-P., 2018. An evaluation of SMOS L-band vegetation optical depth (L-VOD) data sets: high sensitivity of L-VOD to above-ground biomass in Africa. Biogeosciences 15, 4627–4645.

Saatchi, S.S., Harris, N.L., Brown, S., Lefsky, M., Mitchard, E.T., Salas, W., Zutta, B.R., Buermann, W., Lewis, S.L., Hagen, S., 2011. Benchmark map of forest carbon stocks in tropical regions across three continents. Proc. Natl. Acad. Sci. 108, 9899–9904.

Schaefer, G.L., Cosh, M.H., Jackson, T.J., 2007. The USDA natural resources conservation service soil climate analysis network (SCAN). J. Atmos. Ocean. Technol. 24, 2073–2077.

Schmugge, T.J., O'Neill, P.E., Wang, J.R., 1986. Passive microwave soil moisture research. IEEE Trans. Geosci. Remote Sens. GE-24 (1), 12–22.

Serreze, M.C., Clark, M.P., Frei, A., 2001. Characteristics of large snowfall events in the montane western United States as examined using snowpack telemetry (SNOTEL) data. Water Resour. Res. 37, 675–688.

Sheffield, J., Goteti, G., Wen, F., Wood, E.F., 2004. A simulated soil moisture based drought analysis for the United States. J. Geophys. Res. D Atmos. 109, 1–19.

Silva, C.A., Duncanson, L., Hancock, S., Neuenschwander, A., Thomas, N., Hofton, M., Dubayah, R., 2021. Fusing simulated GEDI, ICESat-2 and NISAR data for regional aboveground biomass mapping. Remote Sens. Environ. 253, 112234.

Smith, A.B., Walker, J.P., Western, A.W., Young, R.I., Ellett, K.M., Pipunic, R.C., Richter, H., 2012. The Murrumbidgee soil moisture monitoring network data set. Water Resour. Res. 48 (7).

Su, Z., Wen, J., Dente, L., van der Velde, R., Wang, L., Ma, Y., Yang, K., Hu, Z., 2011. The Tibetan Plateau observatory of plateau scale soil moisture and soil temperature (Tibet-Obs) for quantifying uncertainties in coarse resolution satellite and model products. Hydrol. Earth Syst. Sci. 15, 2303–2316.

Tagesson, T., Fensholt, R., Guiro, I., Rasmussen, M.O., Huber, S., Mbow, C., Garcia, M., Horion, S., Sandholt, I., Holm-Rasmussen, B., 2015. Ecosystem properties of semiarid savanna grassland in West Africa and its relationship with environmental variability. Glob. Chang. Biol. 21, 250–264.

Tian, F., Brandt, M., Liu, Y.Y., Verger, A., Tagesson, T., Diouf, A.A., Rasmussen, K., Mbow, C., Wang, Y., Fensholt, R., 2016. Remote sensing of vegetation dynamics in drylands: evaluating vegetation optical depth (VOD) using AVHRR NDVI and in situ green biomass data over West African Sahel. Remote Sens. Environ. 177, 265–276.

Tian, F., Wigneron, J.P., Ciais, P., Chave, J., Ogee, J., Penuelas, J., Raebild, A., Domec, J. C., Tong, X., Brandt, M., Mialon, A., Rodriguez-Fernandez, N., Tagesson, T., Al-Yaari, A., Kerr, Y., Chen, C., Myneni, R.B., Zhang, W., Ardo, J., Fensholt, R., 2018. Coupling of ecosystem-scale plant water storage and leaf phenology observed by satellite. Nat. Ecol. Evol. 2, 1428–1435.

Tong, X., Brandt, M., Yue, Y., Ciais, P., Rudbeck Jepsen, M., Penuelas, J., Wigneron, J.-P., Xiao, X., Song, X.-P., Horion, S., Rasmussen, K., Saatchi, S., Fan, L., Wang, K., Zhang, B., Chen, Z., Wang, Y., Li, X., Fensholt, R., 2020. Forest management in southern China generates short term extensive carbon sequestration. Nat. Commun. 13798.

Tuttle, S., Salvucci, G., 2016. Empirical evidence of contrasting soil moisture–precipitation feedbacks across the United States. Science 352, 825–828.

Wang, M., Fan, L., Frappart, F., Ciais, P., Sun, R., Liu, Y., Li, X., Liu, X., Moisy, C., Wigneron, J.P., 2021. An alternative AMSR2 vegetation optical depth for monitoring vegetation at large scales. Remote Sens. Environ. 263, 112556.

Wigneron, J.P., Kerr, Y., Chanzy, A., Jin, Y., 1993. Inversion of surface parameters from passive microwave measurements over a soybean field. Remote Sens. Environ. 46 (1), 61–72.

Wigneron, J.-P., Waldteufel, P., Chanzy, A., Calvet, J.-C., Kerr, Y., 2000. Two-dimensional microwave interferometer retrieval capabilities over land surfaces (SMOS mission). Remote Sens. Environ. 73, 270–282.

Wigneron, J.-P., Laguerre, L., Kerr, Y.H., 2001. A simple parameterization of the L-band microwave emission from rough agricultural soils. IEEE Trans. Geosci. Remote Sens. 39, 1697–1707.

Wigneron, J.P., Kerr, Y., Waldteufel, P., Saleh, K., Escorihuela, M.J., Richaume, P., Ferrazzoli, P., de Rosnay, P., Gurney, R., Calvet, J.C., Grant, J.P., Guglielmetti, M., Hornbuckle, B., Mätzler, C., Pellarin, T., Schwank, M., 2007. L-band microwave emission of the biosphere (L-MEB) model: description and calibration against experimental data sets over crop fields. Remote Sens. Environ. 107, 639–655.

Wigneron, J.P., Jackson, T.J., O'Neill, P., De Lannoy, G., de Rosnay, P., Walker, J.P., Ferrazzoli, P., Mironov, V., Bircher, S., Grant, J.P., Kurum, M., Schwank, M., Munoz-Sabater, J., Das, N., Royer, A., Al-Yaari, A., Al Bitar, A., Fernandez-Moran, R., Lawrence, H., Mialon, A., Parrens, M., Richaume, P., Delwart, S., Kerr, Y., 2017. Modelling the passive microwave signature from land surfaces: a review of recent results and application to the L-band SMOS & SMAP soil moisture retrieval algorithms. Remote Sens. Environ. 192, 238–262.

Wigneron, J.-P., Fan, L., Ciais, P., Bastos, A., Brandt, M., Chave, J., Saatchi, S., Baccini, A., Fensholt, R., 2020. Tropical forests did not recover from the strong 2015–2016 El Niño event. Sci. Adv. 6 eaay4603.

Wigneron, J.P., Li, X., Frappart, F., Fan, L., Al-Yaari, A., De Lannoy, G., Moisy, C., 2021. SMOS-IC data record of soil moisture and L-VOD: historical development, applications and perspectives. Remote Sens. Environ. 254, 112238.

Xing, Z., Fan, L., Zhao, L., De Lannoy, G., Frappart, F., Peng, J., Wigneron, J.P., 2021. A first assessment of satellite and reanalysis estimates of surface and root-zone soil moisture over the permafrost region of Qinghai-Tibet Plateau. Remote Sens. Environ. 265, 112666.

Zacharias, S., Bogena, H.R., Samaniego, L., Mauder, M., Fuß, R., Pütz, T., Frenzel, M., Schwank, M., Baessler, C., Butterbach-Bahl, K., Bens, O., Borg, E., Brauer, A., Dietrich, P., Hajnsek, I., Helle, G., Kiese, R., Kunstmann, H., Klotz, S., Munch, J.C., Papen, H., Priesack, E., Schmid, H.P., Steinbrecher, R., Rosenbaum, U., Teutsch, G., Vereecken, H., 2011. A network of terrestrial environmental observatories in Germany. Vadose Zone J. 10, 955–973.

Zeng, J., Chen, K.-S., Cui, C., Bai, X., 2020. A physically based soil moisture index from passive microwave brightness temperatures for soil moisture variation monitoring. IEEE Trans. Geosci. Remote Sens. 58, 2782–2795.

Zwieback, S., Colliander, A., Cosh, M.H., Martínez-Fernández, J., McNairn, H., Starks, P. J., Berg, A., 2018. Estimating time-dependent vegetation biases in the SMAP soil moisture product. Hydrol. Earth Syst. Sci. 22 (8), 4473–4489.